Molecules to Diagnose Young Stellar Objects: The LOMASS Database

Comparing HCO$^+$ (4−3) and H$_2$O (1_{10}−1_{01}) transitions in low-mass protostars

Jaya Ramchandani

in pursuit of

Master of Astronomy
Sterrewacht Leiden, Leiden University

Supervised by

MSc. Umut A. Yıldız
Prof. Dr. Ewine F. van Dishoeck

September 2012

Abstract

To further star and planetary formation studies, it is important to trace the physical and chemical evolution of gas and dust in star forming regions. This thesis introduces the LO-MASS database, a public web-based archive of single-dish submillimetre spectra of molecules observed in young stellar objects by the astrochemistry group at Sterrewacht Leiden. The database will host observations from the James Clerk Maxwell Telescope and the Atacama Pathfinder EXperiment telescope for 22 molecules across 30 low-mass protostar sources. The immediate scientific benefit of LOMASS is public access to a large collection of line observations to compare and evaluate star formation models. LOMASS is currently populated with HCO^+ $(4-3)$ transition data. Using the HCO^+ $(4-3)$ data from LOMASS, this thesis analyses the central spectra of sources at different evolutionary stages (12 Class 0 and 13 Class I sources), and compares the results with those obtained for an optically thicker H_2O $(1_{10}-1_{01})$ line for the same sources. Water is a key tracer of dynamics and chemistry in low-mass star-forming regions, especially outflows and jets, and HCO^+ is a known tracer for envelope and protostellar collapse. The aim of the comparison is to investigate whether HCO^+ traces the same trends as observed for H_2O. A narrow emission of HCO^+ is observed in the 25 sources under comparison, while water is dominated by profiles with broad and medium emissions. Both molecules show inverse and regular P-Cygni profiles, indicative of infalling and expanding envelopes, respectively. The behaviour of HCO^+ follows that of water in terms of its presence in the quiescent envelope, absorption layer, and infalling envelope for both Class 0 and Class I sources. For water, the peak temperature T_{MB}^{peak}, line width Δv_{max}, and integrated intensity $\int T_{MB}\,dv$ all decrease from Class 0 to I, while for HCO^+, similar values are found for T_{MB}^{peak}, a slight decrease in Δv_{max} and an increase in $\int T_{MB}\,dv$ is found. The error margins need to be taken into consideration for a more detailed analysis. Both H_2O but HCO^+ are present and excited in the outflow cavity wall where expansion occurs and in the infalling envelope. Expansion is detected in more Class I than Class 0 sources for both H_2O but HCO^+ and infall is detected in more Class 0 than Class I sources for both H_2O but HCO^+. To form a complete picture of the role of water and other molecules in star formation, further studies are required with a larger sample size of molecular profiles. The LOMASS database is expected to serve as a useful means to this end.

Table of Contents

Chapter 1: Introduction

The study of the life cycle of a star, from birth to death, involves complex observational diagnostics encompassing the entire electromagnetic spectrum. For instance, stars form within dark clouds of gas and dust, and are difficult to detect in optical wavelengths. During the early stages of star formation, the radiation that stars emit are absorbed by the surrounding material, causing the dust to warm up and radiate in the infrared. Therefore, stars at their very early stages of evolution can be observed indirectly at the infrared (IR) and submillimetre (submm) wavelengths. Progress in stellar evolution theories has, consequently, moved hand in hand with technological advances in observational techniques.

At the turn of the 20th century, it was widely believed that stars live forever and that the origin of stars is a part of cosmology. This view changed with the theory of stellar evolution born in 1950, which showed that stars do not live forever and young star formation is still going on. From the 1950s to 1960s, late-type stars were discovered by observing H emission lines, which turned out to be low-mass pre-main sequence stars. Detailed studies on pre-main sequence evolution and cloud collapse were made by mapping interstellar clouds in HI and CO. It was found that these giant molecular clouds (GMCs) contained more mass than needed to form a single star or even a group of stars and had masses up to 10^6 $M_\odot$. OB stars were soon detected near interstellar clouds with possible systematic age variations (van Dishoeck Spring 2011 Lecture Notes).

By the 1980s, Herbig-Haro objects were discovered that displayed high proper motions (optical jets) and bipolar outflows, as mapped with CO. In addition, IRAS satellite maps of clouds at various submm wavelengths presented a distribution of young stellar objects (YSOs) in clouds and their evolutionary sequence. From the 1980s to the early 1990s, developments in ground-based millimetre, submm and IR wavelength observations provided indirect evidence of massive disks around young T-Tauri stars. By the 1990s, astronomers gained definite proof of the existence of disks around young stars through millimetre interferometry and Hubble Space Telescope (HST) imaging (van Dishoeck Spring 2011 Lecture Notes).

In this chapter, the main concepts of low-mass star formation and the spectral evolution of YSOs are discussed. This is followed by a brief overview of the observational benefits at submm wavelengths. This chapter then discusses how molecules are used as a diagnostic tool to study the structure and evolution of YSOs. The line profiles indicating collapse and expansion of the molecular envelope are presented, followed by a brief background of water and HCO^+ as diagnostic molecules in low-mass protostars. This chapter concludes with the goal and organization of this thesis.

1.1 Low-Mass Star Formation

Low-mass stars are defined as stars with a characteristic bolometric luminosity of less than 100 $L_\odot$ and masses of less than ~2 $M_\odot$ (van Dishoeck 2011). Figure 1.1 illustrates the star formation process of low-mass YSOs until they enter the pre-main sequence. Low-mass stars

have a complex physical structure, characterised by a protostellar envelope, bipolar outflow, circumstellar disk, central star and surrounding cloud. They form in GMCs starting with the formation of clumps within these clouds arising due to inhomogeneities. The gas and dust contract under their own gravitation and evolve toward a spherical configuration called the central protostar. The cloud core collapses from inside-out, leaving the protostar with a sur-rounding nebular disk at the centre, which is deeply embedded in a thick envelope (Shu et al. 1977).
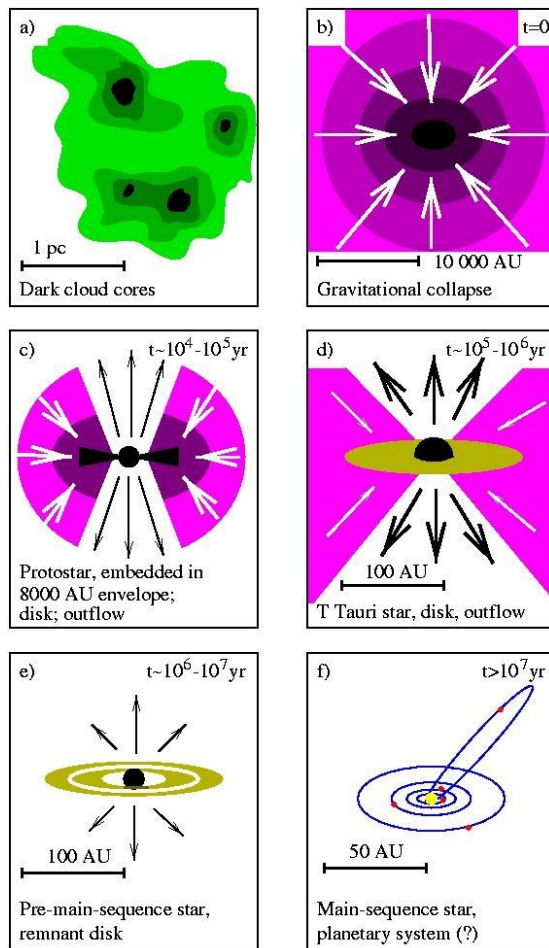
Figure 1.1: Overview of star formation (Hogerheijde 1998, after Shu et al. 1987)

The envelope holds the bulk of the material that accretes onto the central protostar. The tem-perature and density structure within the protostellar envelope can be roughly characterized with a power law, and the density and temperature increase towards the centre as the cloud collapses. This is important because for stars to form, an increase in density of 20 orders of

magnitude needs to be accompanied by an increase in temperature of only 6 orders of magnitude, which is possible through self-gravitational collapse of matter. Wide-angle and high-velocity winds originate close to the central star and carry away the excess angular momentum, allowing further accretion. The outflows impact the surrounding material, producing shocks observed almost a parsec away from the central star. Outflows are easier to detect because the velocity differences are large, of the order of 10 to 200 km/s, over a large area of at least 5000 AU. The early stages of protostars tend to have the most collimated outflows. The infalling material falls towards a plane that is perpendicular to the central star's axis of rotation, forming a circumstellar disk in the later stages: the first steps of planet formation. The central star accretes material rapidly contributing to the bulk of the radiation emitted in the early stages (van Dishoeck Spring 2011 Lecture Notes).

The envelope eventually disperses through two mechanisms: (1) the infalling envelope of gas and dust continues to accrete matter on the growing central protostar and disk and (2) stellar winds break out along the rotational axis of system, reversing infall and sweeping material into two outwardly expanding shells of gas and dust through jets or bipolar outflow. Infall continues in the equatorial regions. The outflow angle opens up with time, terminating infall and presenting a newly formed star with a circumstellar disk that can be viewed optically (called the T-Tauri phase).

Lada (1987) provided a classification scheme for YSOs through infrared observations of several hundreds of YSOs between 1 and 100 μm. The shape of the spectral energy distributions (SED) of an object is closely related to its physical characteristics. The scheme is based on the spectral index, α_{IR}, evaluated between 2.2 and 10−60 μm:

$$\alpha_{IR} = -d \log v \, F_v / d \log v \qquad (1)$$

YSOs have been categorized into four classes under two phases: protostars and pre-main sequence stars (Figure 1.2). A protostar is defined as an object that derives most of its luminosity from accretion of gas and dust, and not nuclear burning. The SED of protostars are dominated by emission from cold dust and peak in the submm and far IR (FIR). A pre-main sequence star is where the surrounding material has been incorporated into the young star and its SED peaks in the optical and near IR. The evolutionary sequence $0 \rightarrow I \rightarrow II \rightarrow III$ proceeds by gradual dispersion of the envelope and disk. The main differences between the classes are outlined below (van Kempen 2008):

- **Class 0:** The SED of Class 0 objects is steep and is well fit by a single temperature blackbody curve ($T_\alpha \propto 40$ K). This is because of their optically thick nature where the received radiation is reprocessed by the gas and dust of the envelope. Class 0 objects are often undetected at near- and mid-IR wavelengths as the bulk of the final stellar mass is not yet assembled. They are associated with a well-collimated outflow, which is the feature that is usually detected first. Extremely high velocity (EHV) bullets are also observed along with chemical anomalies.
- **Class I:** Class I objects are optically invisible and are associated with protostars. Their SED is much broader than a single blackbody curve and is characterised by a

double peak ($\alpha_{IR} > 0$). FIR emission is detected from the envelope, following a power law, while mid-IR emission is detected from the circumstellar disk. Poorly collimated, classic outflow accelerating with distance is detected. The shell structure has with an evacuated cavity and no chemical anomalies.

- **Class II:** The SED of Class II objects is broader than a blackbody, and $-2 < \alpha_{IR} < 0$. It has been successfully modelled as originating from circumstellar disks associated with T-Tauri stars. Class II objects are optically visible and luminosity is radiated in each annulus of the disk. If the disk has a temperature structure $T(R) \propto R^{-n}$, the frequency of the maximum emission scales as $\nu \propto T(R)$. Less outflow is observed for later phases.

- **Class III:** The SED of a Class III object is equivalent to a blackbody with $T \sim 4000$ K. The spectral index corresponds to a reddened zero main sequence star (ZAMS) photosphere ($\alpha_{IR} < -2$).
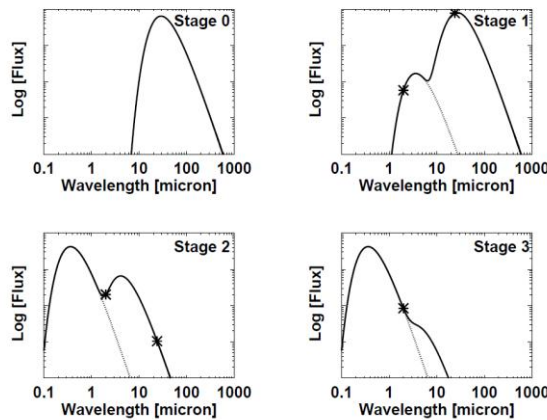

Figure 1.2: Typical SEDs of different stages in low-mass star formation (van Kempen 2008), which correspond to the classes defined by Lada (1999).

1.2 Submillimetre Line Observations

In order to observe star formation, a combination of observing tools is required. For instance, cold molecular clouds emit the bulk of their radiation at FIR or longer, while accretion of material onto the protostellar surface produces emission at the UV and visible wavelengths. Nuclear burning contributes to emission at the extreme UV and possibly X-ray emission. The surrounding envelope absorbs the incoming radiation and converts it into emission at FIR and submm wavelengths. Submm observations are considered the best way to study continuum radiation from low-mass YSOs from the ground. Dense clouds in particular are an excellent playground to observe millimetre emissions from rotational transitions or infrared absorption from vibrational transitions (Figure 1.3).

Pure rotational lines of molecules can be observed in emission at submm wavelengths (0.4−1 mm; 200−800 GHz; 10−100 K excitations). However, only molecules that have a permanent

electric dipole moment can be observed while symmetric molecules like H_2 and N_2 cannot. We know from quantum mechanics that the level spacing scales with $BJ(J + 1)$, where J is the rotational quantum number and B is the rotational constant (van Dishoeck 2009); therefore, the lowest transitions of lighter hydrides occur at submm or FIR wavelengths, while those of heavier molecules occur at longer wavelengths.
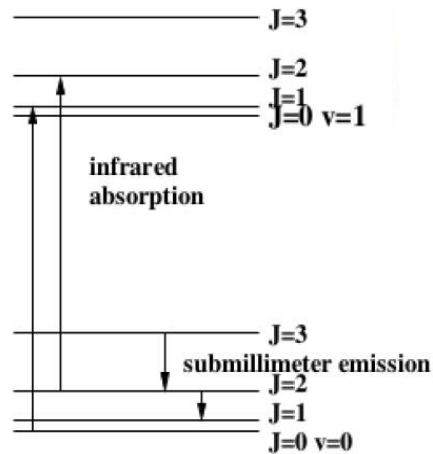

Figure 1.3: IR absorption from vibrational transitions and submm emission from rotational transitions (van Dishoeck & Hogerheijde 1999)

Molecular lines are especially useful in probing the velocity structure of gas. In particular, molecules with strong rotational lines are used as tracers and to distinguish between quiescent, infalling, rotating, and outflowing gas, and higher transitions probe higher temperatures and densities. The line strength tells us about the abundance of the molecule; the line ratios give information on the temperature and density, while the line profile tells us about the kinematics.

The physics involved in understanding astronomical observations are derived from the radiative transfer equation:

$$I_v = I_v(0)e^{-\tau_v} + \int S_v(x)e^{-\tau_v(x)}\mathrm{dx} \qquad (2)$$

where I_v is the received intensity, $I_v(0)$ represents the main radiation source extincted along a line of sight with optical depth τ_v, and S_v represents the intensities originating along the path x at frequency v. Solving the radiative transfer equation gives us a thorough description of the protostellar structure and gas and dust characteristics, through both line and continuum emission. Continuum radiation is typically integrated over a wide frequency range while line radiation is sampled with channel widths of a certain frequency. Line observations of a molecule depend on the level populations and on the incident radiation. Therefore, to solve the line

radiative transfer including molecular excitation, it is necessary for radiative transfer models to account for the temperature and densities dependencies with radius. In order to describe a source through line observations, we need to make certain assumptions about the structure of the source. This can be achieved through a combination of modelling steps and observation simulations (van Kempen 2008).

1.3 Molecules as Diagnostics

Molecules are found throughout the universe: in molecular clouds, stars, protoplanetary disks, stellar and planetary atmospheres, comets, galaxies, and other astronomical objects. About 150 species have been identified in star forming regions so far, with about three species added per year for the past 30 years (Herbst 2008). These include simple diatomic molecules such as CO; ordinary molecules such as NH_3, H_2O, H_2, CO, and CH_3CH_2OH; complex organic molecules such as CH_3OCH_3 as well as exotic molecules like HCO^+, N_2H^+, and HCCCCCCCN (Herbst & van Dishoeck 2009). Polycyclic aromatic hydrocarbons (PAHs) have been found in star forming regions throughout our universe and heavy elements have been found in ices in the coldest and densest clouds (Tielens 2008).

Molecules serve as excellent diagnostics of temperature, density, and velocity within a star forming system. A key question for studies of astrochemistry to answer is what is the evolution of molecules in the universe from formation during the early stages of the universe to the formation of solar systems, and how can molecules be used as physical and chemical diagnostics to probe our universe.

Studies on the astrochemistry of protostellar environments have revealed the chemical characteristics of YSOs (van Dishoeck et al. 2007). Figure 1.4 illustrates the chemical evolution of star forming regions. Pre-stellar cores and the outer cold envelope are characterised by low-T chemistry and heavy freeze-out. Submm diagnostics help us identify ions and deuterated and simple molecules (N_2H^+, H_2D^+ in pre-stellar cores and N_2H^+, HCO^+, H_2CO in the outer cold envelope) while through IR observations, astronomers have detected simple ices (H_2O, CO_2, CO). The inner warm envelope is characterized by evaporation and X-rays (CO^+, OH^+). Submm observations reveal molecules with high extinction temperatures (H_2CO, CH_3OH, CO, CO_2) while IR observations show heated ices as well.

The hot core is characterised by evaporation and high-T chemistry. Submm observations have detected H_2O and complex organics (CH_3OCH_3, CH_3CN) while IR is used to probe the hot gas (HCN, NH_3, HNCO).
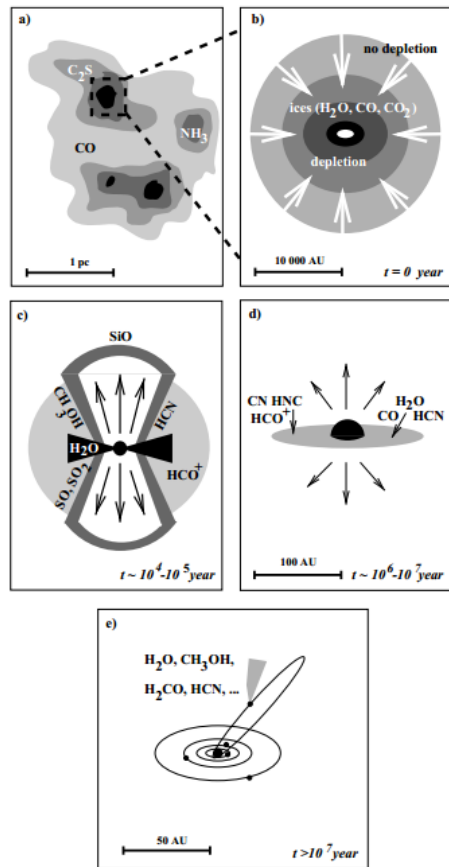
Figure 1.4: Chemical evolution of star forming regions (van Dishoeck and Blake 1998)

The outflows are characterised by shock chemistry, sputtering cores, and sputtering ices. Submm diagnostics have found H_2O, OH, SiO, and SO_2 and ice products such as H_2O, CH_3OH. IR diagnostics have detected H_2 and atomic lines O I, Si II, and S I. The outer disk is characterised by UV irradiation and ion-molecule reactions. Submm observations probe ions and radicals (CN/HCN, HCO^+) and the heavy freeze-out is evidenced by deuterated molecules (DCO^+, H_2D^+). IR observations reveal PAHs and heated ices (NH_4^+). Similar to the hot core, the inner disk is also characterised by evaporation, high-T chemistry, and X-rays (van Dishoeck Spring 2011 Lecture Notes).

1.4 Inside-Out Collapse and the Two-Layer Model

Infall asymmetry is a characteristic signature of line profiles for contracting clouds. It has commonly been observed in cores with highly embedded sources (Myers et al. 1996). We can

infer inward motions using line emission spectra obtained along the line of sight. Infall motion, in principle, can be observed if the foreground of the infalling gas has a lower excitation temperature than the background gas and if the foreground has sufficient optical depth. The indicators are that the line profile will be skewed to the blue, or a double peak will be observed with a stronger blue peak.
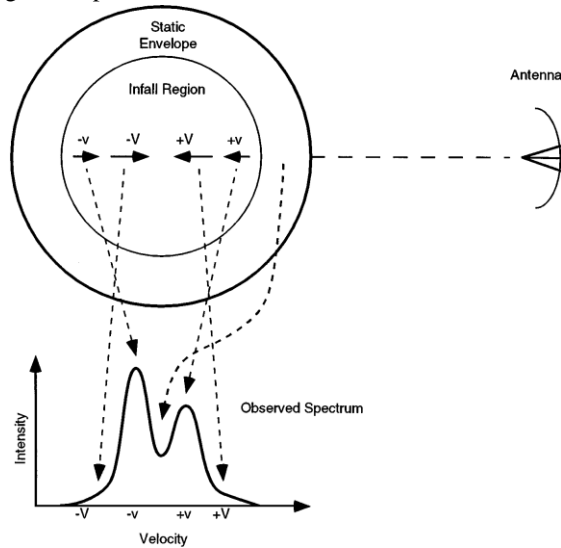

Figure 1.5: Line profile of an inside-out collapse (Evans 1999)

Shu (1977) first proposed a model of inside-out collapse with a self-similar dimensionless solution. The central parts of a sphere that is gravitationally unstable collapses faster than the outer parts. Assuming that the density of the central parts of the core is greater than the outer parts, the free-fall time t_{ff}, which scales with $\rho^{-1/2}$, decreases towards the centre. Consequently, the central parts collapse faster than the outer parts. When spectrally resolved, the line profiles carry information on the absolute values and signs of gas motion along the line of sight. The characteristic emission profile of the protostellar collapse phase is an asymmetric double-peaked line (Figure 1.5). An important pre-requisite for observing such a collapse signature is that the line is optically thick. An optically thin line is difficult to distinguish from a normal emission line without infall/outflow. For optically thick lines, absorption turns the line profile asymmetric because the outer cooler gas in the redshifted wing can partially absorb emission from the hotter shells closer to the protostar. This is not the case for the blueshifted wing because the hotter inner shells are closer to us than the cool outer shells, and the gas temperature increases towards the observer. In the optically thin case, we do not encounter absorption and hence the profile stays symmetric.
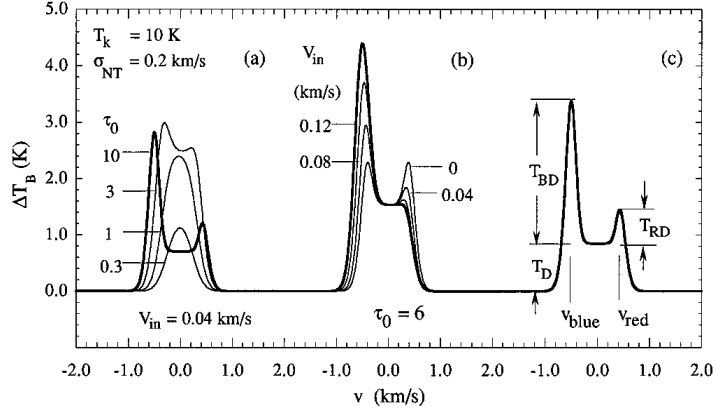
Figure 1.6: Variation of infall asymmetry (a) with peak optical depth τ_0 and (b) with infall speed V_{in} (c) illustrates the definition of various line parameters (Myers et al. 1996)

Myers (1996) proposed a simple two-layer model to characterise infall, involving two uniform layers that approach each other. In this radiative transfer model, the line profile is symmetric for optical depth $\tau_0 < 1$, but its peak skews to the blue as τ increases beyond 1. If the approach speed V_{in} is less than the velocity dispersion σ, the absorption appears as a dip between the brighter blue peak and a fainter red peak. As V_{in} increases, the red peak is absorbed by the foreground layer, which has a lower excitation temperature. For a fixed $\tau_0 > 1$, the blue-red intensity ratio increases until the red peak disappears into the red shoulder or wing while the blue peak becomes brighter. If $V_{in} > \sigma$, the result is two separated peaks of nearly equal strength. The above scenarios are described through the following equation:

$$v_{in} = \frac{\sigma^2}{v_{red} - v_{blue}} \ln\left(\frac{1 + eT_{BD}/T_D}{1 + eT_{RD}/T_D}\right) \qquad (3)$$

where T_D is the brightness temperature of the dip, and T_{BD} and T_{RD} are the heights of the blue and red peaks above the dip, respectively. The line is assumed to be optically thick and σ can be obtained from the full-width half maximum of the line. Figure 1.6 illustrates the set of line parameters used to estimate the infall speed from the line profile. The infall line asymmetry is not limited to the central velocities. The asymmetry can occur in the line wings as long as the emission stays optically thick. Figure 1.7 illustrates the infall line profiles in the starless core L1544 (Tafalla et al. 1998). The lines vary from the high optical depth HCO^+ (1−0) line with strong infall asymmetry to the low optical depth $C^{34}S$ (2−1) line without infall asymmetry.

1.5 HCO⁺ and Water as Tracers

In order to study star formation, it is useful to draw a comparison between an optically thick line such as H_2O ($1_{10}-1_{01}$) (556.936002 GHz) and a less optically thick one such as the HCO^+ (4−3) (356.734288 GHz). Water is a key tracer of dynamics and chemistry in low-mass star-

forming regions, especially outflows and jets, and HCO^+ is a known tracer for the envelope and protostellar collapse.

HCO^+ has been widely studied as a tracer of the envelope of low-mass YSOs, and has been successfully used to show the collapse signature: where optically thick lines show blue asymmetry in the line profile towards the collapse centre and an optically thin lines also appear asymmetric (Mardones et al. 1997, Gregersen et al. 1997, Hogerheijde et al. 1997).

These studies have identified a number of known kinematic infall candidates. Gregersen (2000), in particular, surveyed 23 Class 0 sources in HCO^+ (4−3) and (3−2). Nine sources of the sample showed blue asymmetry, three showed red asymmetry, and one showed different asymmetries in the two lines. HCO^+ was shown to demonstrate the collapse signature well in sources already identified as collapse candidates. Hogerheijde et al. (1997) examined the envelopes of nine embedded YSOs and found HCO^+ (4−3) and (3−2) emission lines in about half of the sources, concentrated towards the source position. The spectra were shown to be best fit with a narrow emission line ($\Delta v \approx 2-5$ km s^{-1}), broad line wings, and narrow self-absorption in some cases. The spectra were well-fit by a single Gaussian at the v_{LSR} of the self-absorption when present.

Water is one of the most important molecules to study star formation. It acts as a strong coolant in protostellar environments, playing an important role in the energy balance. On the other hand, when its levels are pumped by IR radiation and collisional de-excitation, it plays the role of a heating agent as well. Water has so far been found to be the most abundant molecule in icy mantles and is speculated to play a critical role in the formation of planets and other objects in protoplanetary disks. Observations of water from Earth are limited, but the 557 GHz ground state line of water has been studied in detail (van Dishoeck et al. 1996, Boonman et al. 2003, Kristensen et al. 2012). Water is found to show weak emission because of freeze-out on grains in cold clouds and undergoes several orders of magnitude of change in abundance between cold and warm regions. It is considered to act as a 'switch that turns on whenever energy is deposited in molecular clouds' and works as a natural filter for warm gas (van Dishoeck 2009).
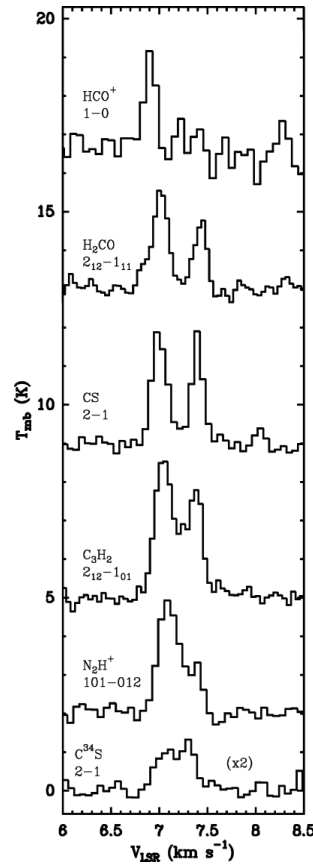

Figure 1.7: Spectral profiles of dense gas tracer lines in Class 0 L1544 (Tafalla et al. 1998).

Kristensen et al. (2012) detected o-H_2O ($1_{10}-1_{01}$) line emission from 28 of 29 low-mass Class 0 (15) and Class I (14) YSOs surveyed as part of the Water in Star Forming Regions with Hershel (WISH) program. The broad line profiles ($\Delta v \approx 100$ km s^{-1}) showed several dynamical components such as regular and inverse P-Cygni profiles indicative of expansion and infall respectively, as well as EHV bullets.

1.6 Goal and Organization of this Thesis

The goal of this thesis is two-fold: to introduce the LOMASS database, a web-based archive of single-dish submm spectra of molecules observed in YSOs thus far by the astrochemistry group at Sterrewacht Leiden, and to use these data to compare the features of the HCO$^+$ (4−3) across 25 low-mass sources with the results obtained for H_2O ($1_{10}-1_{01}$) by Kristensen et al. (2012) for the same sources. In particular, it examines the infall and expansion of the envelope using these two lines as tracers to draw comparisons between Class 0 and Class I sources. Chapter 2 describes the LOMASS database and the data reduction process. Chapter 3 compares the line emissions across 20 molecules and notes the features observed. Chapter 4 discusses the observed features and their implications for infall and expansion from Class 0 to Class I while Chapter 5 concludes this thesis.

Chapter 2: The LOMASS Database

Ongoing technological developments in optical, infrared, and submm astronomy have resulted in a significant amount of data relating to star formation in particular. In today's world of remote data access to perform astronomical research, there is a lack of reliable online databases to add value and complement existing data archives and data published in journals. Over the past decade, the astrochemistry group at Leiden Observatory has obtained a comprehensive and complete data set of several low-mass, Class 0 and Class I, young stellar objects (YSOs) through various research projects.

The Leiden Observatory Single-dish Submm Spectral Database of Low-mass YSOs (LOMASS) database is planned as a public web archive of the reduced line data from the James Clerk Maxwell Telescope (JCMT)[1], the Atacama Pathfinder EXperiment (APEX) telescope[2], and Herschel. This project has been undertaken towards fulfilling one of the long-term goals of molecular astrophysics: to obtain a full inventory of YSOs to further studies on star formation. The spectral data contained herein can be used to study links between the molecular lines and the chemical and physical properties of low-mass YSOs.

The immediate scientific benefit of LOMASS is public access to a large collection of line observations to compare and evaluate star formation models. Further, the data has been reduced, allowing scientists to save valuable time in using the data. The database will provide line data for 22 molecules across the 30 sources listed in Appendix A. In total, the database will host over 360 spectral maps.

2.1 The Sources

LOMASS includes 16 Class 0 and 14 Class I YSOs. Table 2.1 presents an overview of the sources.

2.2 The Telescopes and Receivers

The sources listed in Table 2.1 have been observed with JCMT and APEX. Future additions to the database will include data from other submm facilities including the Herschel Space Observatory, IRAM 30m Telescope, Onsala Space Observatory, and Caltech Submillimeter Observatory.

2.2.1 JCMT

JCMT is the largest submm telescope in the world with a diameter of 15 m. It is mainly used to study interstellar dust and gas, distant galaxies, and our solar system. It is situated at Mauna Kea, Hawaii, at an altitude of 4092 m. The heterodyne receivers, covering the atmospheric

---

[1]The James Clerk Maxwell Telescope (JCMT) is operated by the Joint Astronomy Centre on behalf of the Science and Technology Facilities Council of the United Kingdom, the Netherlands Organisation for Scientific Research, and the National Research Council of Canada.

[2]This publication is based on data acquired with the Atacama Pathfinder Experiment (APEX). APEX is a collaboration between the Max-Planck-Institut fur Radioastronomie, the European Space Observatory, and the Onsala Space Observatory.

Table 2.1: LOMASS source details

Source	Class[a]	RA (h m s)	Dec (° ' ")	v_{LSR} (km/s)	D (kpc)	L_{bol} ($L_\odot$)	T_{bol} (K)	M_{env} ($M_\odot$)
B335	0	19 37 00.9	+07 34 09.6	8.4	0.25	3.42	39	1.2
BHR71	0	12 01 36.3	−65 08 53.0	−4.4	0.2	14.5	48	3.1
Ced110IRS4	0	11 06 47	−77 22 32.4	4.2	0.125	0.8	56	0.17
DKCha	1	12 53 17.2	−77 07 10.6	3.1	0.178	35	593	0.8
Elias29	1	16 27 9.4	−24 37 19.6	4.3	0.125	19.8	391	0.04
GSS30IRS1	1	16 26 21.4	−24 23 4.0	3.5	0.125	13.8	144	0.17
HH100	1	19 01 49.1	−36 58 16.0	5.6	0.125	17.7	256	8.14
HH46	1	8 25 43.9	−51 0 36.0	5.2	0.45	27.9	104	4.36
IRAS15398	0	15 43 1.3	−34 09 15.0	5.1	0.13	1.6	52	0.47
NGC1333-IRAS2A	0	03 28 55.6	+31 14 37.1	7.7	0.25	35.7	50	5.13
NGC1333-IRAS3A	1	03 29 3.0	+31 16 4.0	8.5	0.25	41.8	149	9.47
NGC1333-IRAS4A	0	03 29 10.5	+31 13 30.9	7	0.25	9.1	33	5.59
NGC1333-IRAS4B	0	03 29 12.0	+31 13 8.1	7.1	0.235	4.4	28	3
L1157	0	20 39 6.4	+68 02 13	2.6	0.325	5.5	42	1.48
L1448MM	0	03 25 38.9	+30 44 5.4	5.2	0.25	8.4	52	3.91
L1489	1	04 04 43.0	+26 18 57.0	7.2	0.14	3.4	234	0.18
L1527	0	04 39 53.9	+26 03 9.8	5.9	0.14	1.4	78	0.92
L1551IRS5	1	04 31 34.1	+18 08 5.0	6.2	0.14	23.5	109	2.32
L483	0	18 17 29.9	−04 39 39.5	5.2	0.25	10.2	49	4.4
L723MM	0	19 17 53.7	+19 12 20.0	11.2	0.3	3.6	39	1.32
OphIRS63	1	16 31 35.6	−24 01 29.6	2.8	0.125	1.3	327	0.25
RCrAIRS5	1	19 01 48.0	−36 57 21.6	5.7	0.13	7.1	126	2
RNO91	1	16 34 29.32	−15 47 1.4	0.5	0.125	2.6	339	0.45
Ser-SMM1	0	18 29 49.6	+01 15 20.5	8.5	0.25	30.4	39	16.13
Ser-SMM3	0	18 29 59.2	+01 14 0.3	7.6	0.23	5.1	38	3.2
Ser-SMM4	0	18 29 56.6	+01 13 15.1	8	0.25	1.9	26	2.11
TMC1	1	04 41 12.4	+25 46 36.0	5.2	0.14	0.62	181	0.2
TMC1A	1	04 39 34.9	+25 41 45.0	6.6	0.14	2.4	169	0.22
TMR1	1	04 39 13.7	+25 53 21.0	6.3	0.14	2.5	145	0.23
VLA1623	0	16 26 26.4	−24 24 30.0	4.2	0.125	2	36	0.66

Note: The source characteristics are the latest update of WISH sources (van Dishoeck et al. 2011) obtained from Kristensen et al. (2012), Yıldız et al. (in prep), and Kristensen et al. (in prep). [a] Class 0 sources are characterised as YSOs with bolometric temperature $T_{\mathrm{bol}} < 70$ K (Evans et al. 2009)

windows between 215 and 680 GHz, are mounted in the cabin while the continuum bolometer array instrument, SCUBA-2, and the heterodyne array receiver, HARP, occupy the Nasmyth platforms.

The heterodyne receivers detect the characteristic submm radiation that molecules emit when they rotate, which tell us about the temperature, density, and motion of the gas. The receivers operate in three frequency bands, known as A, B, and D in order of increasing frequency. (The C-band receiver RxW(C), operating from 425 to 510 GHz, has been discontinued.) The basic characteristics of these systems are given below (Table 2.2).

Table 2.2: JCMT receiver system

Receiver system	A (RxA3)	B (HARP)
Tuning range (GHz)	211−279	325−375
Beamwidth (HPBW, arcsec)	20	14
Beam Efficiency	0.69	0.63

Source: JCMT website

HARP-B, the key receiver used for the JCMT observations in LOMASS, is a 16 element heterodyne array receiver with a 2' × 2' field of view. It covers the 345 GHz band, where CO (3−2) and HCO$^+$ (4−3) transitions can be observed along with emission lines of methanol, formaldehyde and other species (van Kempen 2008).

2.2.2 APEX

The Atacama Pathfinder Experiment (APEX) is a collaboration between Max Planck Institut für Radioastronomie (MPIfR), Onsala Space Observatory (OSO), and the European Southern Observatory (ESO) to construct and operate a modified ALMA prototype antenna as a single dish on the high altitude site of Llano de Chajnantor. APEX is built to study cold dust and gas in our own and in distant galaxies. Using APEX, we can improve our understanding of the structure and chemistry of planetary atmospheres, dying stars, regions of star formation and distant starburst galaxies by tracing the thermal continuum emission and analysing high frequency spectral lines. The details of the past and present receivers are presented in Table 2.3.

Table 2.3: APEX receiver system

Instrument	Type	Frequency (GHz)	HPBW (arcsec)	IF range (GHz)
APEX-1(SHeFI)	Heterodyne SIS	211−275	30−25	4−8
APEX-2(SHeFI)	Heterodyne SIS	275−370	23−17	4−8
APEX-3(SHeFI)	Heterodyne SIS	385−500	17−13	4−8
APEX-T2(SHeFI)	Heterodyne HEB	1250−1390	5	2−4
LABOCA	Bolometer array	345	19	
SABOCA	Bolometer array	850	8	
APEX-2A	Heterodyne SIS	279−381	18	4−8

Source: APEX website

The CHAMP$^+$ array receiver also provides good coverage of the submm atmospheric windows. It is a unique 2×7 element heterodyne receiver and works simultaneously in high-frequency 690 and 800 GHz bands. Its state of the art detectors allow the observation of high-J lines of molecules such as CO. APEX-CHAMP$^+$ provides large-scale velocity resolved maps at resolutions of <10" resolution, which can be used to complement data from other telescopes.

2.3 Data Reduction

The data are placed on the Lithium server at Sterrewacht Leiden under the following location: /lomass/sources. The folder contains individual folders with the object names, with sub-folders under them with the molecular line names (Figure 2.1). The data for a particular molecular line is placed in these sub-folders. This consistent format allows easy retrieval of data for the web interface scripts.
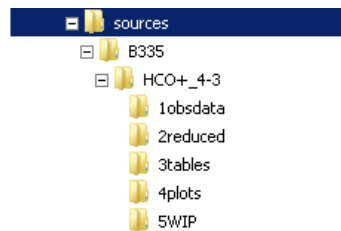

Figure 2.1: Folder structure to retrieve data

The data were reduced and analysed using the CLASS program of the GILDAS software package. The reduction script has 10 parts, which are described below. The script sources information from the following two database files, which are also in class format:

1. LowMassdb.class: This file contains the updated values for the source velocity v_{LSR}, RA, and Dec for all 30 sources.
2. LowMassdbFrequencies.class: This file contains the updated rest frequency and Einstein coefficients for the HCO$^+$ (4−3) line at 356.734288 GHz. As more lines are added to the database, this list needs to be updated.

The entire script used to reduce the HARP_B HCO$^+$ (4−3) line observation is located at /lomass/scripts, and its function is summarized here.

Script 0: The first step of the reduction is to prepare a consistent folder structure, with five sub-folders:

- 1obsdata: This folder contains the original RAW files along with the source name and line name extracted as .dat files from the folder structure.
- 2reduced: The datacube, reduced data, and FITS file for the central spectrum are placed in this folder, which are the output of scripts 4, 6, and 7, respectively.
- 3tables: The table used to generate the contour intensity map of the source is placed here along with key values extracted from the central spectrum for analysis: source name, line

18

name, source velocity v_{LSR}, root mean square (rms), main beam peak temperature $T_{\text{MB}}^{\text{peak}}$, full width at half maximum Δv_{max} and integrated intensity $\int T_{\text{MB}} dv$ (and the ranges of integration)

- 4plots: The central spectrum and contour intensity map in EPS and PNG formats are placed here and linked to the web interface.
- 5WIP: Work in progress files are stored here for checks and troubleshooting

Script 1: Sometimes some of the detectors have broken pixels, which causes inconsistent data. This script marks empty pixels as *Not a Number* (NaN) data to exclude it from the map and further data processing.

Script 2: The baseline is then removed from the continuum subtracted spectra using the `BASE` command. This script also modifies the beam efficiency to 1.0 using Ruze's equation:

$$B_{\text{eff}}(\lambda) = B_0 e^{\left[\frac{4\pi\sigma}{\lambda}\right]^2} \tag{5}$$

where B_0 is the scaling factor with no units (between 0 and 1), and σ the width factor in microns.

Script 3: The spectra are then resampled and the velocity resolution is set to 0.2 km s^{-1} for consistency among data sets. The beam efficiency is modified to 0.63 for JCMT and 0.73 for APEX observations. The rest frequency and line name are updated from LowMassdb.class to a consistent format.

Script 4: An LMV spectra cube is then created with an associated weight image from an XY table. To convolve the beam size for further analysis, the map beam and resolution should be changed in this part of the script.

Script 5: As some data comes in multiple observation files (e.g., JCMT ACSIS data), this script writes a combined observation file (JCMT Das and APEX usually have only one observation file)

Script 6: Another check is performed for data consistency after the files are combined

Script 7: The central spectrum is then extracted and converted to FITS format

Script 8: The single central spectrum details are extracted by fitting a single Gaussian: rms, $T_{\text{MB}}^{\text{peak}}$, Δv_{max} and $\int T_{\text{MB}} dv$ (and the ranges of integration)

Script 9: The table used to generate the contour intensity map of the source is extracted

Script 10: A number of temporary files are created through the reduction process, and this script cleans up the folder by deleting the temporary files

2.4 Access and Interface

The LOMASS database can be accessed through the URL http://lomass.strw.leidenuniv.nl/. It provides a brief introduction to the project and allows you to search by object or by molecular line (Figure 2.2). The selection list is currently populated with the molecular lines of interest to the astrochemistry group by Leiden University. Only the molecular line data for HCO^+ (4−3) have been reduced and uploaded. The remaining lines will be reduced and put online by September 2013. The dropdown lists have been populated with the objects and molecular lines listed in Appendix A.
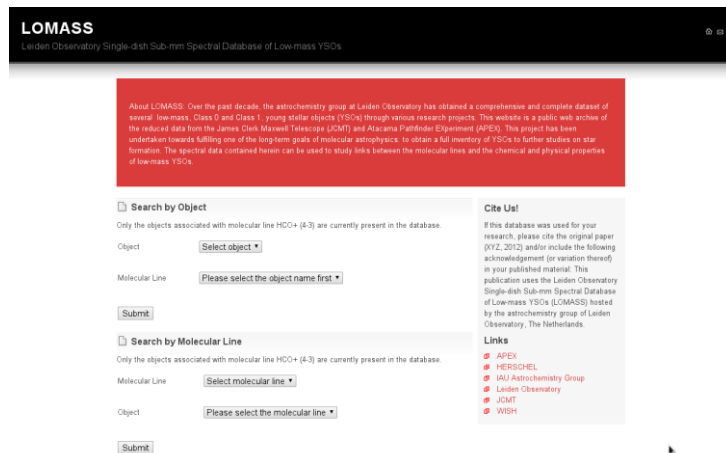
Figure 2.2: LOMASS database homepage

The submit page presents the following features (Figure 2.3):
- Central spectrum and contour intensity map
- Source details including the object name, line, class, RA, and Dec
- Central spectrum details including the rest frequency, rms, T_{MB}^{peak}, Δv_{max} and $\int T_{MB}dv$ (and the ranges of integration)
- Downloads of the reduced JCMT / APEX data, the central spectrum in FITS format, and the central spectrum and contour intensity map in EPS format.

The central spectrum and contour intensity maps for the HCO^+ (4−3) emission line for 26 sources are listed in Appendix B.

2.5 Future Perspectives

The aim is to make the LOMASS database a fully automated system to enter RAW data and automatically reduce it and add it to the online web interface. The following activities are planned to be completed by September 2013. This would involve the optimisation of scripts to 100% automation across telescopes to automatically
- reduce raw data (with a web-embedded CLASS script)
- generate plots (with a python script)
- add entry into a SQL database
- add entry into dropdown on homepage
- generate display page (in php)

An SQL backend will be used to store the data. A web form to add a new source, molecular line, and other details will be available for registered users to add new data. In addition, a correlation plotter (graphing) tool is planned to draw easy correlations among the extracted data for the sources and molecular lines.
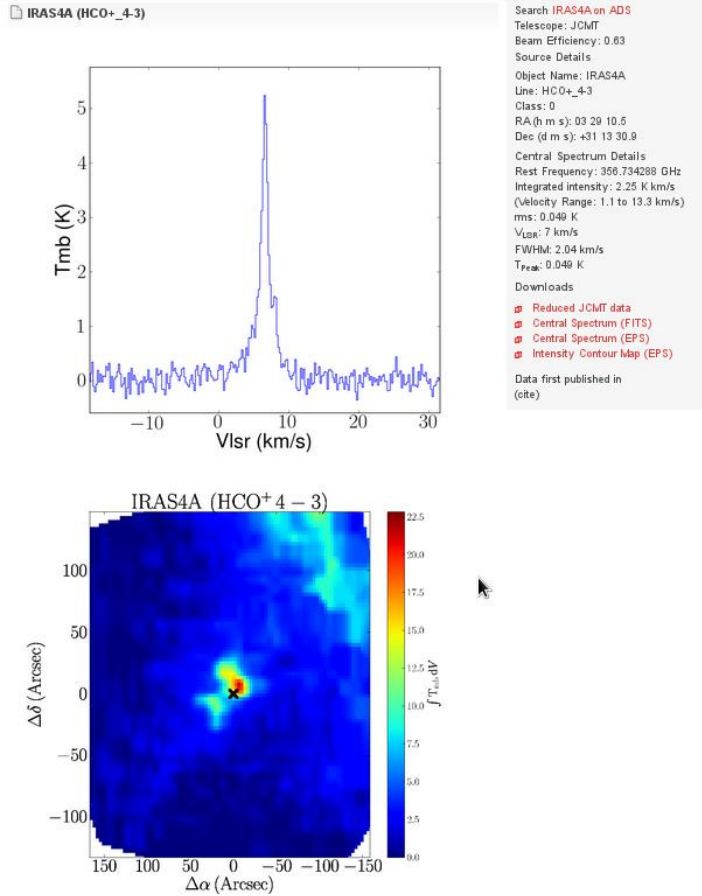
IRAS4A (HCO+_4-3)

$IRAS4A\ (HCO^+\ 4-3)$

Figure 2.3: Source and molecular line details

21

Chapter 3: HCO⁺ (4−3) Observations and Results

This chapter examines the HCO$^+$ (4−3) line emissions present in the LOMASS database, noting the prominent features. The results are presented in this chapter, while the discussion (see Chapter 4) compares the results with those obtained for H_2O ($1_{10}-1_{01}$) by Kristensen et al. (2012).

3.1 HCO⁺ (4−3) Sources

The LOMASS database contains 26 sources with the HCO$^+$ (4−3) emission line, as listed in Table 3.1.Twenty-five of these sources overlap with the sources selected by Kristensen et al. (2012) including 12 Class 0 sources and 13 Class I sources[3]. The central spectrum was fitted with a single Gaussian and the root mean square (rms), peak temperature of the main beam T_{MB}^{peak}, full width half maximum (Δv_{max}), and integrated intensity ($\int T_{MB} \, dv$) have been extracted.

Table 3.1: HCO$^+$ (4−3) source and central spectrum details

Source Name	rms (mK)	T_{MB}^{peak} (K)	Δv_{max} (km s^{-1})	$\int T_{MB} \, dv$ (K km s^{-1})	Integration range (km s^{-1})
B335[a]	0.09	4.8	1.1	5.7	[4.2, 12.6]
Ced110IRS4[b]	0.91	4.2	1.8	5.4	[1.6, 6.8]
DKCha[b]	0.2	1.8	1.2	2.1	[−1.2, 7.4]
Elias29 [a]	0.25	1.6	2.1	3	[1.9, 7.5]
GSS30IRS1[a]	0.13	9.9	1.5	16.7	[−1.6, 8.6]
HH46[b]	0.72	3.9	1.4	4.9	[4, 7.8]
HH100[b]	0.86	5.8	1.4	5.8	[3.6, 7.8]
IRAS15398[a]	0.25	2.1	1.3	2.4	[0.5, 9.7]
NGC1333-IRAS2A[a]	0.12	2.6	2.0	4.7	[−3.4, 8.6]
NGC1333-IRAS3A[a]	0.2	4.8	1.1	6.5	[1.1, 9.3]
NGC1333-IRAS4A[a]	0.23	1.9	2.8	4.1	[−0.3, 14.7]
L1157[a]	0.23	7.1	1.7	8.4	[0.5, 11.3]
L1448MM[a]	0.32	7.2	1.4	11.1	[2.4, 12]
L1489[a]	0.1	4.4	1.0	5.5	[1.1, 9.3]
L1527[a]	0.1	2.3	2.0	4.8	[5.2, 17.2]
L1551IRS5[a]	0.35	3.6	3.7	7.4	[−1.7, 17.1]
L483[a]	0.17	6.2	1.8	12.3	[3, 14]
L723MM[a]	0.05	1.0	2.0	2.2	[1.1, 13.3]
OphIRS63[a]	0.2	0.8	1.1	0.9	[−1.3, 6.9]
RNO91[a]	0.29	6.0	0.8	5.2	[−3.1, 4.1]
Ser SMM1[a]	0.13	4.7	6.5	20.3	[−6.5, 23.5]
Ser SMM4[a]	0.08	10.2	2.3	25.7	[1.4, 14.6]
TMC1[a]	0.23	3.2	1.0	3.2	[1.3, 9.1]
TMC1A[a]	0.22	1.2	2.0	1.5	[0.7, 12.5]
TMR1[a]	0.21	4.1	1.1	5.1	[2, 10.6]

[a]Observed with JCMT, beam efficiency 0.63

[a]Observed with APEX, beam efficiency 0.73

---

[3] The excluded source is VLA1623. Its central spectrum and intensity map have been presented in Appendix B.

3.2 HCO⁺ (4−3) Observed Features

The central spectra of 25 sources under comparison are presented in this section. The most prominent features of the profiles are (a) narrow emission, defined as $\Delta v_{\mathrm{max}} < 5$ km s^{-1} (b) self-absorption, centred at source velocity; (c) regular P-Cygni profile characterised by a combination of an emission and a blueshifted absorption; and (d) an inverse P-Cygni profile characterised by a combination of an emission and a redshifted absorption. Figure 3.1 presents one example of each feature with for HCO⁺ (4−3).
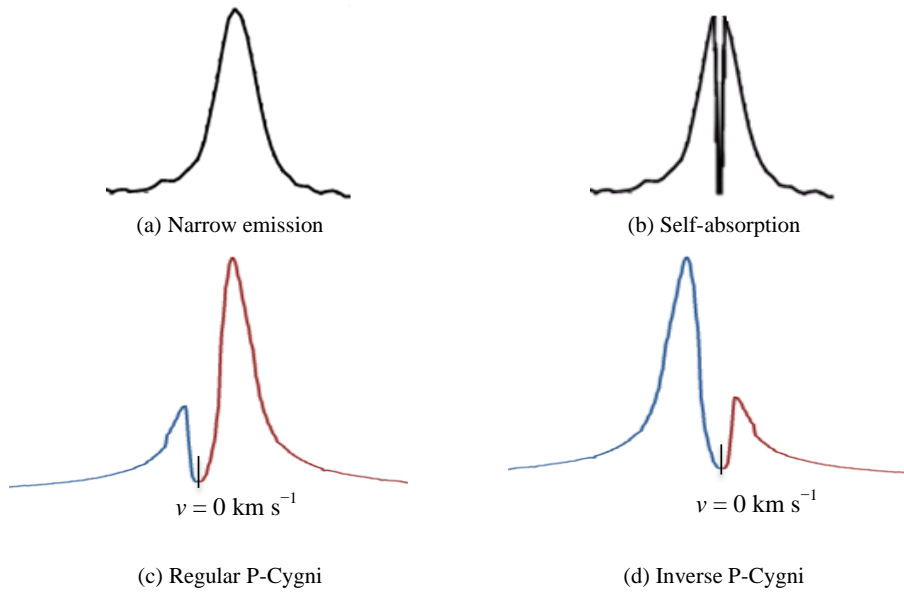

(a) Narrow emission   (b) Self-absorption

$v = 0$ km s^{-1} $v = 0$ km s^{-1}

(c) Regular P-Cygni   (d) Inverse P-Cygni

Figure 3.1: Line shapes of features for HCO⁺ (4−3) (a) narrow emission, (b) self-absorption, (c) P-Cygni, and (d) inverse P-Cygni.

The central spectra of all 25 sources were fitted with a single Gaussian (green line) and the residual of the fit (blue) has been presented in Figures 3.2−3.6, in the order given in Table 3.1. It should be noted that the absorption features were masked in the following sources before the Gaussian fit: B335, Elias29, HH46, HH100, IRAS15398, NGC1333-IRAS2A, NGC1333-IRAS4A, L723MM, L1157, L1489, L1527, L1551IRS5, SMM1 and SMM4. The results are as follows:

1. A narrow emission is observed in all sources.
2. 10 of 12 Class 0 sources showed a self-absorption feature (83%), while only 6 of 13 Class I sources showed a self-absorption feature (46%).
3. Regular or inverse P-Cygni profiles are detected in sources where narrow emission and absorption are seen next to each other, centred at source velocity.
4. Inverse P-Cygni profiles were detected in 8 of the 12 Class 0 sources, and regular P-Cygni profiles were detected in 2. For the Class I sources, inverse P-Cygni profiles were detected in 4 of 13 sources and a regular P-Cygni profile was only detected in one source.

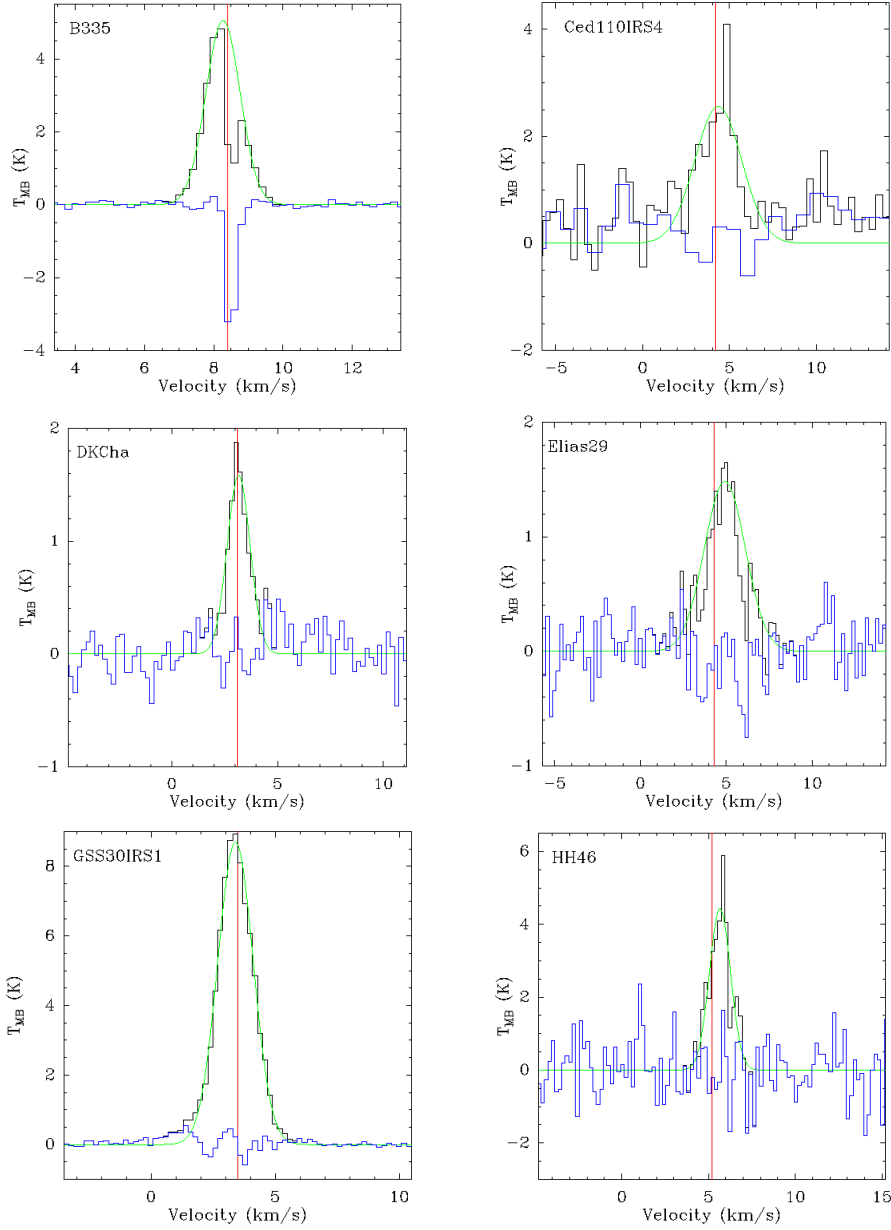These features have been summarized in Table 4.1 of the discussion.

Figure 3.2 HCO^+ (4−3) JCMT and APEX spectra (black line) at the central position of low-mass sources fitted with a single Gaussian (green line) and showing the residual of the fit (blue line). The red line marks the source velocity v_{LSR} as listed in Table 2.1.
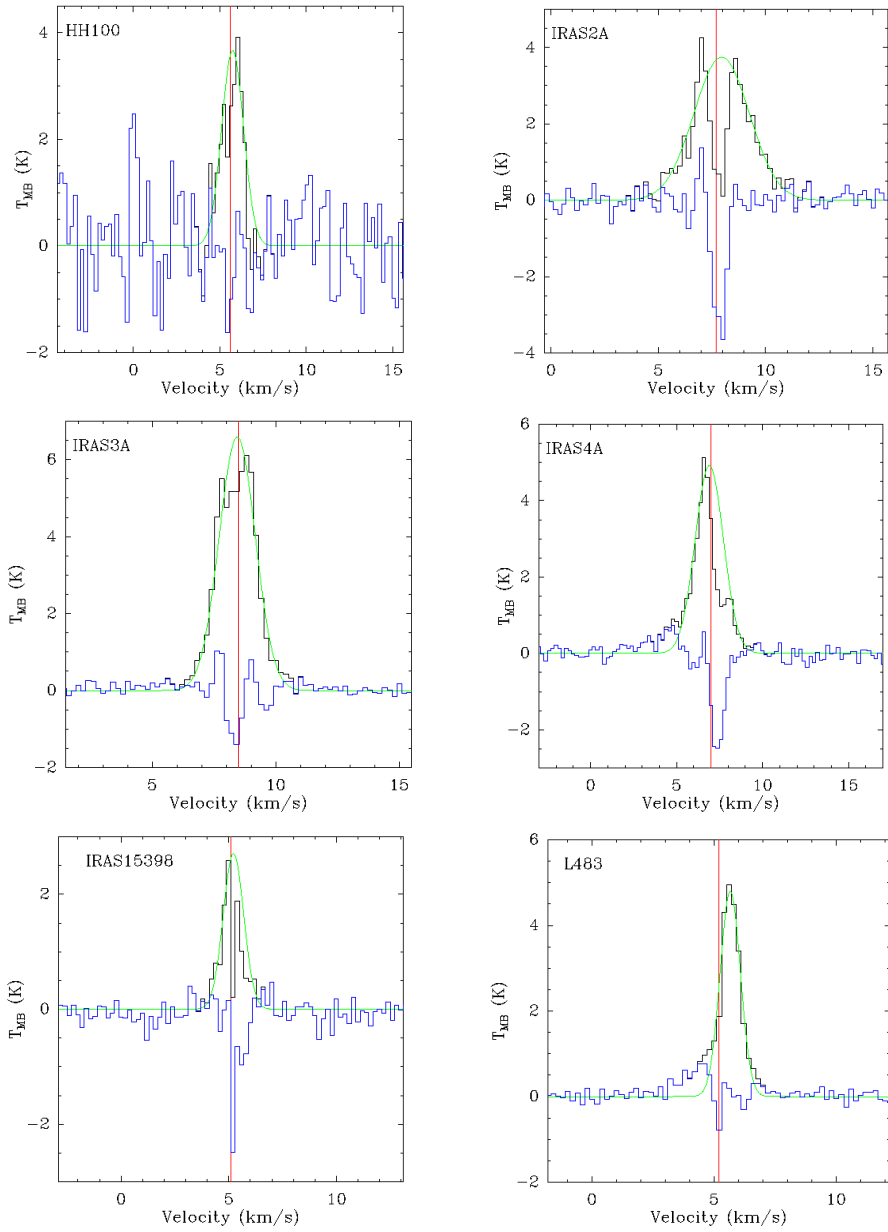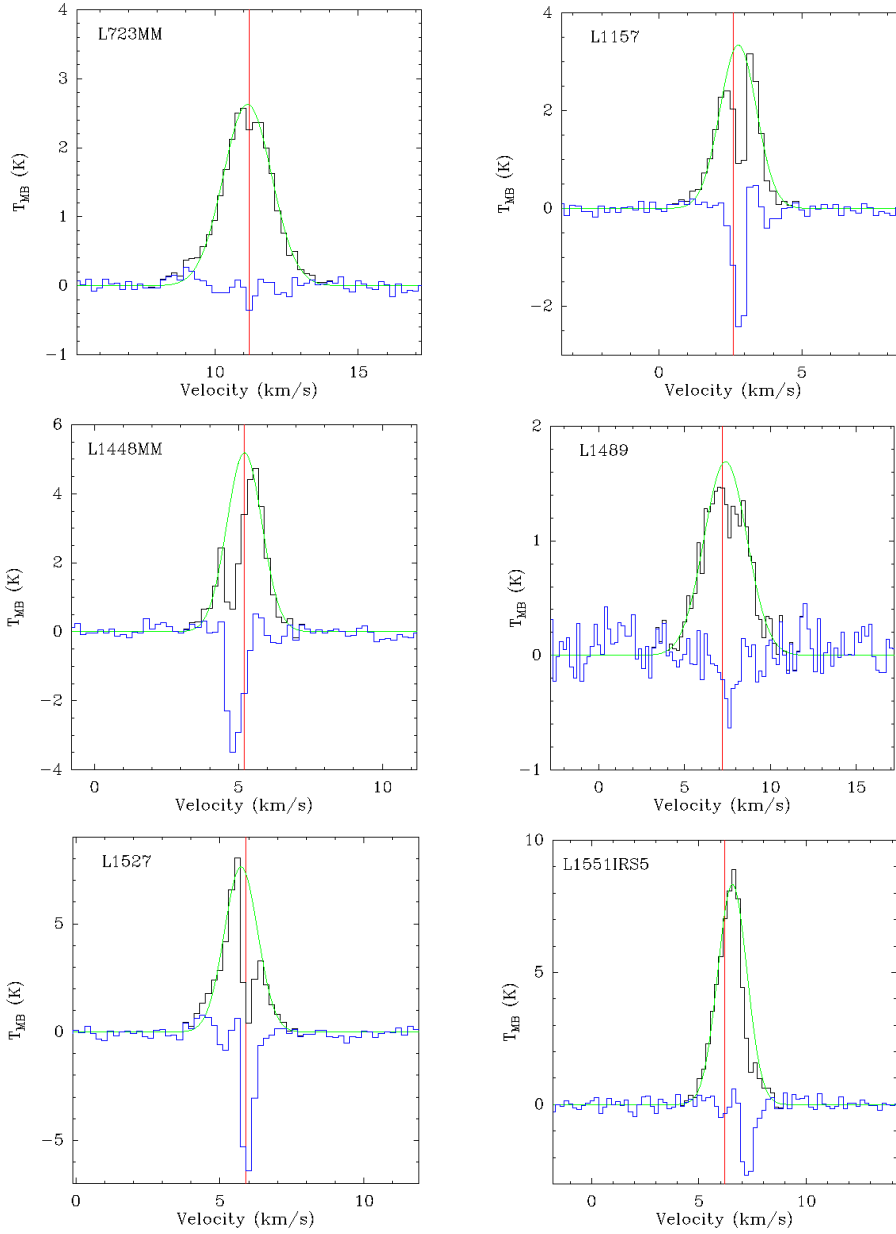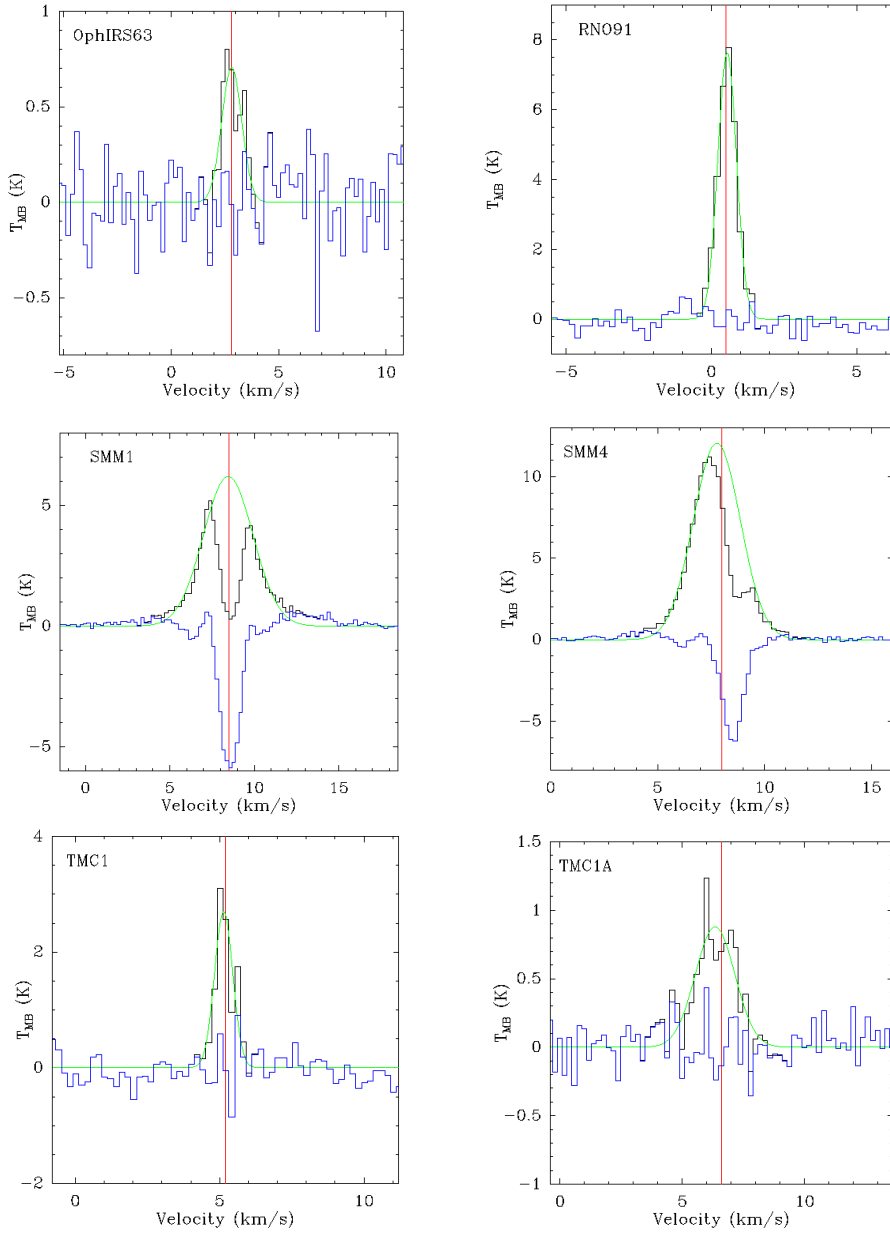
Figure 3.3 Same as 3.2

25

Figure 3.4 Same as 3.2
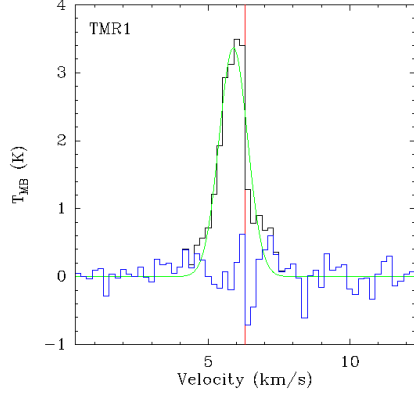
26

Figure 3.5 Same as 3.2

27

Figure 3.6 Same as 3.2

3.3 HCO⁺ (4−3) Correlations

In order to understand the origin of HCO^+ emission, we compare the total HCO^+ integrated line intensity $\int T_{MB}\, dv$, scaled to a common distance of 200 pc, to the bolometric temperature T_{bol}, bolometric luminosity L_{bol}, envelope mas   s M_{env}, and Δv_{max} of the line (Figure 3.7).
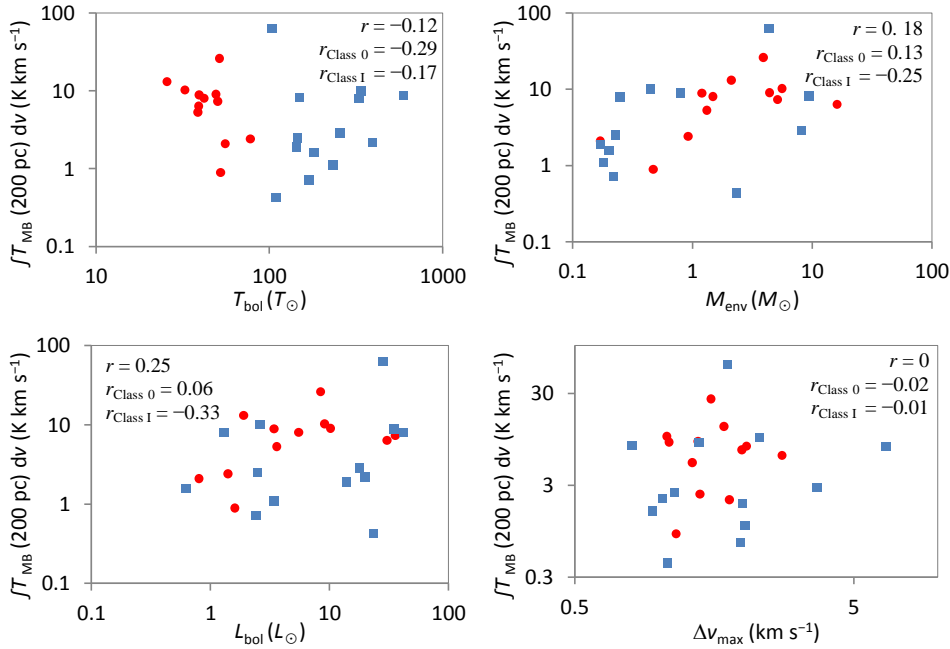

Figure 3.7: Correlation plots showing the integrated HCO^+ (4−3) line intensity scaled to a common distance of 200 pc as a function of various physical parameters: T_{bol}, L_{bol}, M_{env}, and Δv_{max}. Class 0 sources are marked in red circles and Class I sources in blue squares.

Following Kristensen et al. (2012), this study quantitatively examines the comparison using Pearson's correlation coefficient, r. The results are presented in Table 3.1. The correlations

28

were also compared separately for Class 0 and Class I sources. Values of $r \approx 1$ implies a strong correlation, $r \approx 0$ implies no correlation, and $r \approx -1$ implies a strong anti-correlation. Correlations, defined as $|r| > 0.7$, are not observed for any of the cases listed in Table 3.1.

Chapter 4: Discussion

This chapter compares the results presented in Chapter 3 with those for H_2O ($1_{10}-1_{01}$) obtained by Kristensen et al. (2012) for the same sources. Among the 29 sources surveyed by Kristensen et al., the four sources excluded from comparison are NGC1333-IRAS4B, BHR71, Ser SMM3, and RCrA-IRS5A because of lack of HCO^+ (4−3) transition data for these objects.

4.1 Comparing HCO⁺ (4−3) and H₂O (1₁₀−1₀₁) Observed Features

Table 4.1 compares the features observed for HCO^+ (4−3) with the narrow, medium, and broad component of H_2O ($1_{10}-1_{01}$) by Kristensen et al. (2012). The behaviour of Class 0 sources differs from that of Class I sources in terms of regular or inverse P-Cygni profiles and absorption and emission components. It should be noted that whenever there is emission in water, there is absorption in HCO^+ and vice-versa for all sources except for RNO91.

The following results are inferred for the 12 Class 0 sources:
1. Four sources exhibit inverse P-Cygni profiles in both HCO^+ (4−3) and H_2O ($1_{10}-1_{01}$): IRAS15398, NGC1333-IRAS4A, L1527, and Ser SMM4.
2. One source, L723MM, exhibits an inverse P-Cygni in HCO^+ (4−3) but a regular P-Cygni for H_2O ($1_{10}-1_{01}$).
3. Three sources exhibit inverse P-Cygni profiles in HCO^+ (4−3) but neither regular nor inverse P-Cygni in H_2O ($1_{10}-1_{01}$): B335, NGC1333-IRAS2A, and Ser-SMM1.
4. Two sources exhibit a regular P-Cygni profile in HCO^+ (4−3): L1157 and L1448MM. For L1157, an inverse P-Cygni profile is detected in H_2O ($1_{10}-1_{01}$). EHV bullets are detected in the H_2O ($1_{10}-1_{01}$) line profiles for both L1157 and L1448MM.
5. None of the sources share a regular P-Cygni profile between the two molecular lines.
6. Two sources do not exhibit regular or inverse P-Cygni profiles for both molecular lines: Ced110IRS4 and L483.

The following behaviour is inferred for the 13 Class I sources:
1. None of the sources exhibit regular or inverse P-Cygni profiles in both lines
2. Four sources exhibit an inverse P-Cygni profile in HCO^+ (4−3), L1551IRS5, OphIRS63, TMC1, and TMC1A. One of them, L1551IRS5, exhibits a regular P-Cygni in H_2O ($1_{10}-1_{01}$). There is no detection of water for TMC1A.
3. One source, NGC1333-IRAS3A, shows a regular P-Cygni profile in HCO^+ (4−3) but none for H_2O ($1_{10}-1_{01}$). IRAS3A also exhibits a medium absorption in H_2O ($1_{10}-1_{01}$) among all the Class I sources.
4. Three sources exhibit regular P-Cygni profiles in H_2O ($1_{10}-1_{01}$): DKCha, HH46, and L1551IRS5. All the three profiles have broad components and the regular P-Cygni profiles are superposed on the outflow components in DKCha and L1551IRS5.
5. One source, GSS30IRS1, exhibits an inverse P-Cygni in H_2O ($1_{10}-1_{01}$) but a symmetric emission in HCO^+ (4−3)
6. Five sources exhibit symmetric profiles in both H_2O ($1_{10}-1_{01}$) and HCO^+ (4−3): Elias29, HH100, L1489, RNO91, TMR1.

Table 4.1: Comparison of observed features in the HCO$^+$ (4−3) and H$_2$O (1$_{10}$−1$_{01}$)[a] line profiles

Object	Class	**R**egular / **I**nverse P-Cygni HCO$^+$ (4−3)	**R**egular / **I**nverse P-Cygni H$_2$O (1$_{10}$−1$_{01}$)	**A**bsorption / **E**mission HCO$^+$ (4−3)	**A**bsorption / **E**mission H$_2$O (1$_{10}$−1$_{01}$)[b]			Bullets H$_2$O (1$_{10}$−1$_{01}$)
					Narrow	Medium	Broad	
B335	0	I	-	E+A	E	-	E	
Ced110IRS4	0	-	-	E	A	E	-	
IRAS15398	0	I	I	E+A	E+A	E	-	
NGC1333-IRAS2A	0	I	-	E+A	A	E	E	
NGC1333-IRAS4A	0	I	I	E+A	E+A	E	E	
L1157	0	R	I	E+A	E+A	-	E	X
L1448MM	0	R	-	E+A	A	-	E	X
L1527	0	I	I	E+A	E+A	-	E	
L483	0	-	-	E	A	E	-	
L723MM	0	I	R	E+A	E+A	E	-	
Ser SMM1	0	I	-	E+A	A	E	E	
Ser SMM4	0	I	I	E+A	E+A	-	E	
DKCha	1	-	R	E	E+A	-	E	
Elias29	1	-	-	E	E+A	E	-	
GSS30IRS1	1	-	I	E	E+A	E	-	
HH100	1	-	-	E+A	E	E	-	
HH46	1	-	R	E	E+A	-	E	
NGC1333-IRAS3A	1	R	-	E+A	A	A	E	
L1489	1	-	-	E	A	-	E	
L1551IRS5	1	I	R	E+A	E+A	-	E	
OphIRS63	1	I	-	E+A	-	E	-	
RNO91	1	-	-	E	-	E	-	
TMC1	1	I	-	E+A	-	-	E	
TMC1A	1	I	-	E+A	-	-	-	
TMR1	1	-	-	E	A	E	-	

Note: The line above DKCha divides the Class 0 and Class I sources

[a]Data for H$_2$O (1$_{10}$-1$_{01}$) obtained from Kristensen et al. (2012)

[b]Narrow component $\Delta v < 5$ km s^{-1}; Medium component $5 < \Delta v < 20$ km s^{-1}; Broad component $\Delta v > 20$ km s^{-1}

4.2 Physical Significance

The physical significance of the observed features are discussed here, focussing on the narrow components of H_2O and HCO^+. Table 4.2 presents the percentage of sources exhibiting a particular feature, as listed in Table 4.1. Figure 4.1 is a graphical representation of the table.

Table 4.2: Physical significance and comparison between percentage of Class 0 and Class I sources exhibiting a particular feature. The green and purple arrows show the change from Class 0 to I.

Observed Feature	Physical Significance	H_2O $(1_{10}-1_{01})$ Class 0[a]	H_2O $(1_{10}-1_{01})$ Class I[a]	HCO^+ (4-3) Class 0	HCO^+ (4-3) Class I
Narrow Emission	Quiescent envelope	58.3% ↓	50%	100%	100%
Narrow Self-Absorption	Absorption layer located in front of quiescent envelope	91.7% ↓	61.5%	76.9% ↓	46.2%
Inverse P-Cygni[b]	Infalling envelope	41.7% ↓	7.7%	66.7% ↓	30.8%
P-Cygni[b]	Expanding envelope	8.3% ↑	23.1%	16.7% ↓	7.7%

[a]12 Class 0 and 13 Class I sources in sample
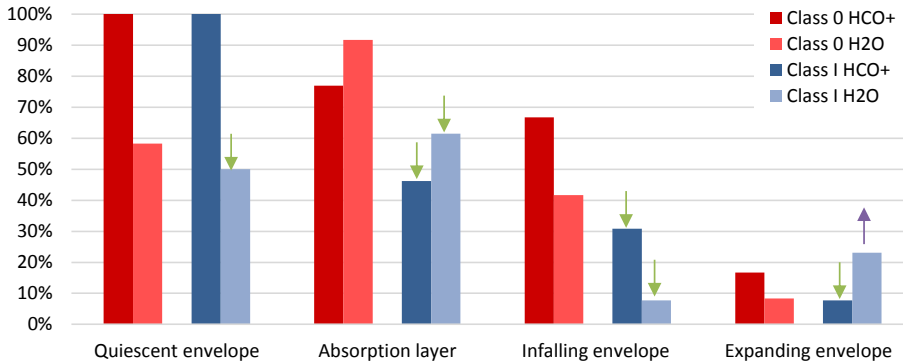[b]Accompanied by narrow absorption and emission at source velocity.

Figure 4.1: Graphical representation of Table 4.2.

The behaviour of HCO^+ follows that of water in terms of its presence in the quiescent envelope, absorption layer, and infalling envelope for both Class 0 and Class I sources. For the expanding envelope, there is a decrease in the number of sources exhibiting the indicative P-Cygni profile for Class 0 sources but an increase in Class I sources exhibiting the profile.

There are some overall trends observed in the average profile parameters between Class 0 and I sources (Table 4.3). For water, T_{MB}^{peak}, Δv_{max}, and $\int T_{MB}\,\mathrm{d}v$ all decrease from Class 0 to I, while for HCO^+, similar values are found for T_{MB}^{peak}, a slight decrease in Δv_{max} and an increase

in T_{MB} dv is found. The error margins need to be taken into consideration for a more detailed analysis.

Table 4.3: Ratio of profile parameters from Class 0 to Class I stages for average Class 0 and I values.

Molecule	T_{MB}^{peak} (K)	Δv_{max} (km s^{-1})	$\int T_{MB}$ dv^b (K km s^{-1})
H_2O $(1_{10}-1_{01})$	0.64	0.48	0.28
HCO^+ (4-3)	1	0.9	1.4

Figures 4.2 and 4.3 compare the regular and inverse P-Cygni profiles of H_2O $(1_{10}-1_{01})$ (Kristensen et al. 2012) where the broad component has been subtracted with the HCO^+ (4-3) line profile for the same sources.

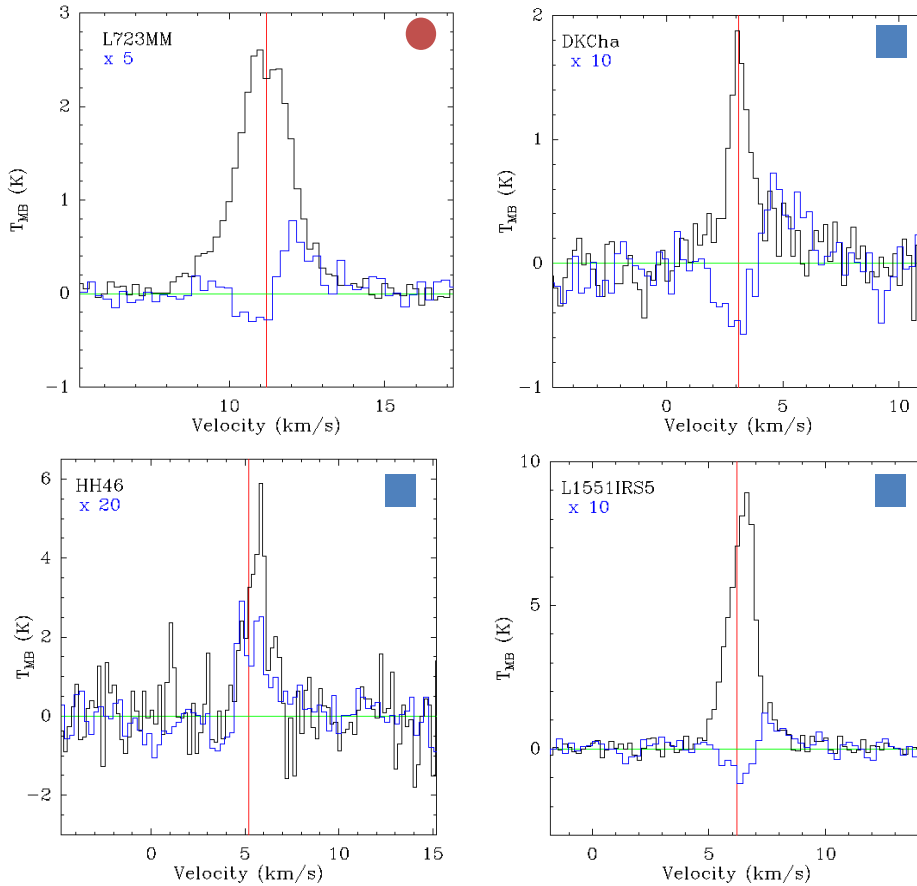**Figure 4.2:** Comparison between regular P-Cygni profiles for H_2O $(1_{10}-1_{01})$ (blue) with the broad component subtracted with the HCO^+ (4-3) line profile (black). The red circle at the top right corner denotes a Class 0 source and the blue square denotes a Class I source. The multiplication factor for the water profile is presented in the top right corner.
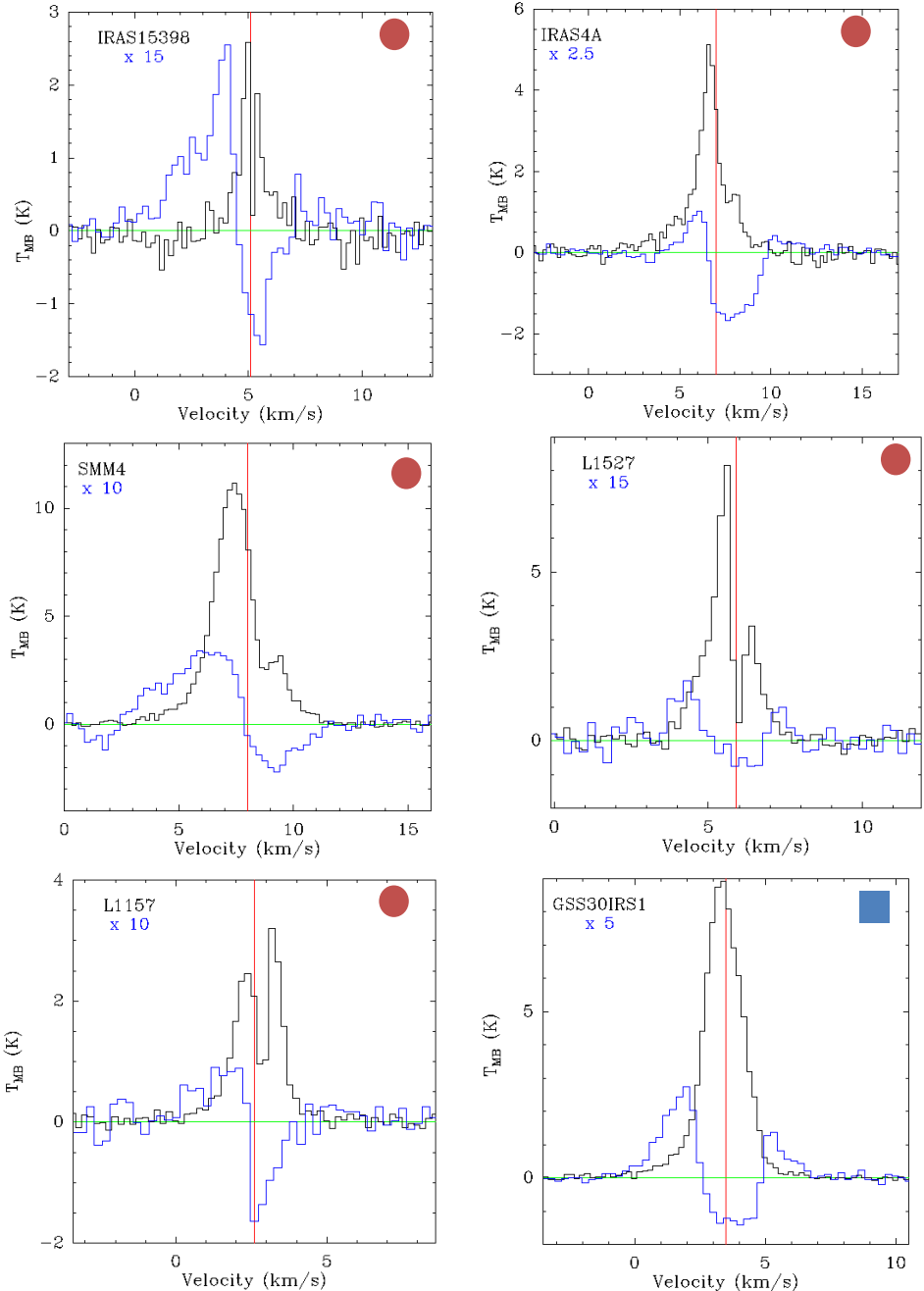
Figure 4.3: Comparison between inverse P-Cygni profiles for H_2O ($1_{10}-1_{01}$) (blue) with the broad component subtracted with the HCO^+ (4-3) line profile (black). The red circle at the top right corner denotes a Class 0 source and the blue square denotes a Class I source. The multiplication factor for the water profile is presented in the top right corner.

One Class 0 source, L723MM, exhibits infall for HCO^+ but expansion for H_2O ($1_{10}-1_{01}$). It should be noted that L723MM is a borderline Class I source (Kristensen et al. 2012). The other three sources that exhibit expansion for HCO^+ also have broad components, indicative of outflow, and the regular P-Cygni profiles are superposed on the outflow components in DKCha and L1551IRS5 (Kristensen et al. 2012). This suggests that both H_2O and HCO^+ are present and excited in the outflow cavity wall where expansion occurs. It should be noted that expansion is detected in more Class I than Class 0 sources for both H_2O and HCO^+.

Four of the 12 Class 0 sources show signs of infall for both HCO^+ and H_2O: IRAS15398, NGC1333-IRAS4A, L1527, and Ser SMM4. For L1157, infall is detected for H_2O but HCO^+ indicates expansion. GSS30IRS1 shows infall for H_2O but emission from the quiescent envelope for HCO^+. The red asymmetry corresponds to an absorption in water in most cases. This could be because of the optically thicker nature of H_2O ($1_{10}-1_{01}$). This suggests that both H_2O but HCO^+ are present and excited in the infalling envelope. Infall is detected in more Class 0 than Class I sources for both H_2O but HCO^+.

4.3 Characterising Infall with the Two-Layer Model

This section investigates whether the same model used for H_2O by Kristensen et al. (2012) can be used to fit the HCO^+ (4-3) (356.734288 GHz) line profiles, for those sources that exhibit inverse P-Cygni in both molecules: IRAS15398, NGC1333-IRAS4A, L1527, and Ser SMM4. The model is based on the equations of Myers et al. (1996).

Table 4.4: Best-fit parameters for the infall modelling of HCO^+ (4-3)

Parameter	NGC1333-IRAS4A	Ser SMM4	IRAS15398	L1527
v_{in} (km s^{-1}) [a]	0.5	1.2	0.3	0.08
$\Delta v(C^{18}O)$ (km s^{-1}) [b]	0.8	1.0	0.5	1.0
σ	1.88	2.35	1.17	2.35
τ_0 [a]	1	1.3	0.9	1.5
Φ [a]	0.3	0.2	0.2	0.15
T_r (K) [a]			15	
T_f (K) [a]			10	
v_{LSR}	7	8	5.1	5.9

[a] From Kristensen et al. (2012) [b] From Yıldız et al. (2012)

Figure 4.4 Observed and model line profiles in IRAS15398, NGC1333-IRAS4A, L1527, and Ser SMM4.

4.4 Correlations between HCO$^+$ (4−3) and H$_2$O (1$_{10}$−1$_{01}$)

Figure 4.5 compares the T_{MB}^{peak}, Δv_{max}, and $\int T_{MB}\, dv$ (scaled to 200 pc) values of the HCO$^+$ (4−3) and H$_2$O (1$_{10}$−1$_{01}$)[4] lines from Kristensen et al. (2012) considering multiple components but excluding the saturated absorption features. No correlation is found for T_{MB}^{peak} and Δv_{max} between the two lines. A correlation is found when comparing $\int T_{MB}\, dv$ values for Class 0 sources ($r_{Class\,0} = 0.78$), but none for Class I and all sources. This implies that as the total integrated intensity of HCO$^+$ (4−3) increases that of H$_2$O (1$_{10}$−1$_{01}$) increases for Class 0 sources.

Further studies are required with a larger number of molecular lines. It would also be useful to correlate the abundances of these two molecules during different stages of the formation process.
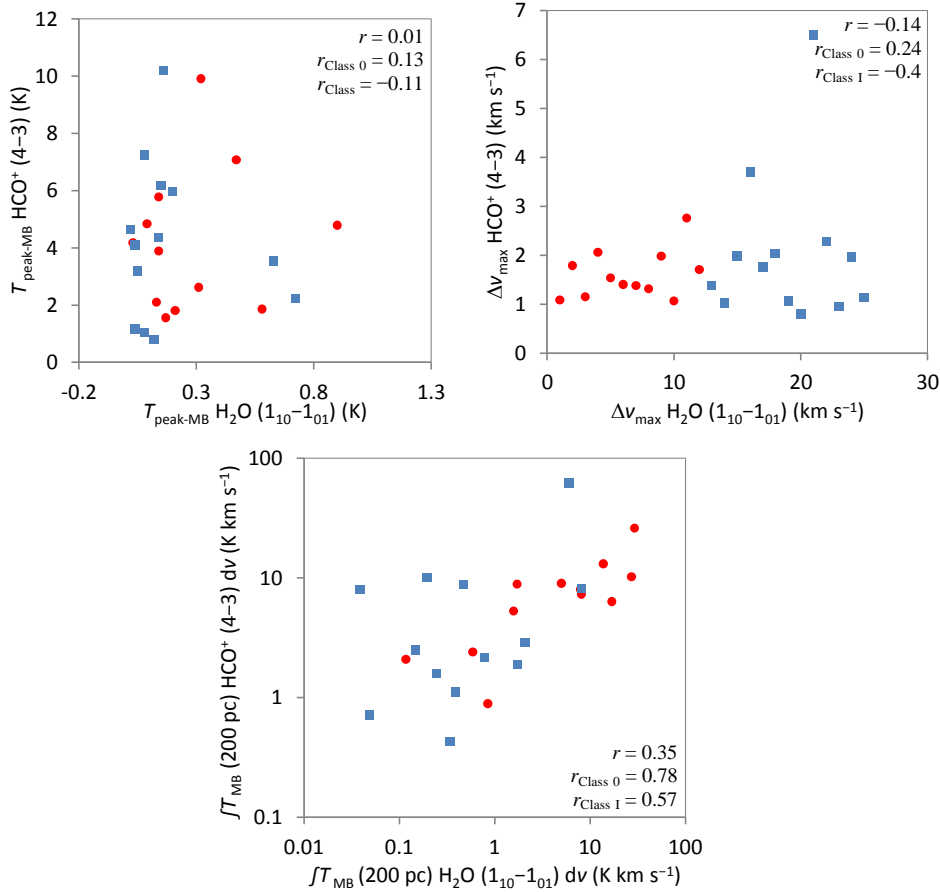

Figure 4.5: Correlation plots comparing T_{MB}^{peak} B, Δv_{max}, and $\int T_{MB}\, dv$ (scaled to 200 pc) HCO$^+$ (4−3) and H$_2$O (1$_{10}$−1$_{01}$). Class 0 sources are marked with red circles and Class I sources with blue squares.

---

[4] Values for H$_2$O (1$_{10}$−1$_{01}$) obtained from Table A.2 in Kristensen et al. (2012)

4.5 Where are the H_2O and HCO^+ transitions coming from?

Kristensen et al. (2012) shows that H_2O profiles are dominated by a broad emission, suggesting that the water emission comes from outflows rather than the quiescent envelope. Inverse P-Cygni profiles in seven sources (six Class 0, one Class I) indicate an infalling envelope and regular P-Cygni profiles in four sources (three Class I, one Class 0) indicate an expanding envelope. Molecular bullets are exclusively detected in Class 0 sources. The water abundance in the cold outer envelope of the order of 10^{-10}, which is low. The different H_2O profile components show an evolutionary trend where Class 0 sources are dominated by outflow components originating inside the infalling envelope. After large scale infall diminishes, the outflow weakens and H_2O emission diminishes.

Figure 4.7 shows where HCO^+ is found and excited (top half of figure) in comparison to where H_2O is found and excited (bottom half) for all the components. In Class I sources, the outflow is less collimated and the envelope is less dense. This would explain the decrease in H_2O and HCO^+ intensity. Further analysis is required to form a complete picture with the distance scales, density profiles and abundance ratios.
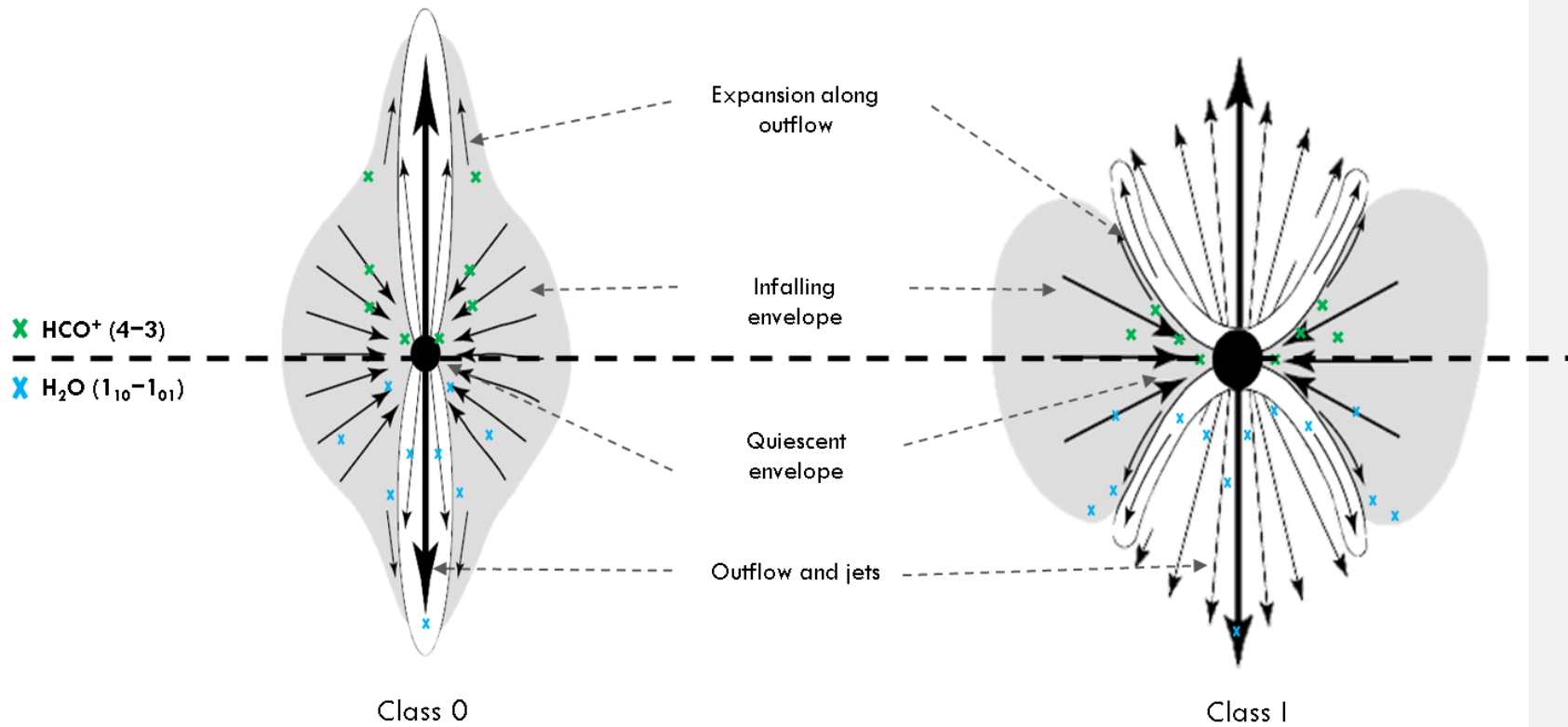
Figure 4.7: HCO^+ found and excited (top half of figure) in comparison to H_2O found and excited (bottom half) as traced by the HCO^+ (4−3) and H_2O ($1_{10}−1_{01}$) rotational lines. All components including the broad component have been mapped. The base figure is taken from Arce & Sargent (2006).

Chapter 5: Conclusion

This thesis introduces the LOMASS database, a web-based archive of single-dish submm spectra of molecules observed in YSOs by the astrochemistry group at Sterrewacht Leiden, designed for researchers to analyse the molecular spectra and draw conclusions to further star formation theories. The database will be publically available by September 2013 after it has been fully automated and populated with over 360 spectral maps.

Using HCO^+ ($4-3$) line data from the LOMASS database, this thesis analyses the central spectra of 25 low-mass sources (12 Class 0 and 13 Class I), and compares the results with those obtained by Kristensen et al. for the optically thicker H_2O ($1_{10}-1_{01}$) line for the same sources. The aim of this thesis is to compare HCO^+ and H_2O line profiles across 25 previously identified low-mass protostars and uncover the role of these molecules and their relation in the evolution from the Class 0 to Class I stage. Water is a key tracer of dynamics and chemistry in low-mass star-forming regions, especially outflows and jets, and HCO^+ is a known tracer for the envelope and protostellar collapse.

The main results are as follows:

1. HCO^+ ($4-3$) line profile analysis
    - A narrow emission of HCO+ ($4-3$) is observed in all 25 sources under comparison.
    - 10 of 12 Class 0 sources showed a self-absorption feature (83%), while only 6 of 13 Class I sources showed a self-absorption feature (46%).
    - Regular or inverse P-Cygni profiles are detected in sources where narrow emission and absorption are seen next to each other, cantered at source velocity.
    - Inverse P-Cygni profiles were detected in 8 of the 12 Class 0 sources, and regular P-Cygni profiles were detected in 2. For the Class I sources, inverse P-Cygni profiles were detected in 4 of 13 sources and a regular P-Cygni profile was only detected in one source.

2. HCO^+ ($4-3$) correlations
    There was no correlation found between $\int T_{MB}\, dv$ scaled to a common distance of 200 pc and T_{bol}, L_{bol}, M_{env}, Δv_{max} for HCO^+ ($4-3$) for all, Class 0 and Class I source groups.

3. Comparing HCO^+ ($4-3$) and H_2O ($1_{10}-1_{01}$) observed features
    - The behaviour of Class 0 sources differs from that of Class I sources in terms of regular or inverse P-Cygni profiles and absorption and emission components.
    - Whenever there is emission in water, there is absorption in HCO^+ and vice-versa for all sources except one Class I source, RNO91. HCO^+ only exhibits a narrow emission while water is dominated by broad and medium emissions.
    - The behaviour of HCO^+ follows that of water in terms of its presence in the quiescent envelope, absorption layer, and infalling envelope for both Class 0 and Class I sources. For the expanding envelope, there is a decrease in the number of sources ex-

39

hibiting the indicative P-Cygni profile for Class 0 sources but an increase in Class I sources exhibiting the profile.

- For water, T_{MB}^{peak}, Δv_{max}, and $\int T_{MB}\,dv$ all decrease from Class 0 to I, while for HCO$^+$, similar values are found for T_{MB}^{peak}, a slight decrease in Δv_{max} and an increase in $T_{MB}\,dv$ is found. The error margins need to be taken into consideration for a more detailed analysis.
- Both H_2O but HCO$^+$ are present and excited in the outflow cavity wall where expansion occurs. Expansion is detected in more Class I than Class 0 sources for both H_2O but HCO$^+$.
- Both H_2O but HCO$^+$ are present and excited in the infalling envelope. Infall is detected in more Class 0 than Class I sources for both H_2O but HCO$^+$.

4. HCO$^+$ (4−3) and H_2O (1_{10}−1_{01}) correlations
   - No correlation found for T_{MB}^{peak} and Δv_{max} between HCO$^+$ (4−3) and H_2O (1_{10}−1_{01}) for all, Class 0 and Class I sources.
   - Correlation found for Class 0 sources comparing $\int T_{MB}\,dv$ (scaled to 200 pc) between HCO$^+$ (4−3) and H_2O (1_{10}−1_{01}) but not for Class I and all sources. This implies that as the total integrated intensity of HCO$^+$ (4−3) increases that of H_2O (1_{10}−1_{01}) increases for Class 0 sources.
   - No correlation between five H_2O (1_{10}−1_{01}) sources showing the narrow component and HCO$^+$ (4−3) line for T_{MB}^{peak}, Δv_{max}, and $\int T_{MB}\,dv$ (scaled to 200 pc).

To form a complete picture of the role of water and other molecules in star formation, further studies are required with a bigger sample size of molecular profiles. The LOMASS database is expected to serve as a useful means to this end.

Acknowledgements

I would like to thank Sterrewacht Leiden for the opportunity to work on this research project. I would especially like to thank my supervisors for their guidance and patience in the completion of this thesis, and Lars Kristensen for his scientific insight. I would also like to thank my friends, family, and the universe at large for their support during this journey.

References

Arce, H. G., & Sargent, A. I. 2006, PA, 646, 1070

Boonman, A. M. S., Doty, S. D., van Dishoeck, E. F., et al. 2003, A&A, 406, 937

Evans, N. J. 1999, ARA&A, 37, 311

Evans, N. J., Dunham, M. M., Jørgensen, J. K., et al. 2009, ApJS, 181, 321

Gregersen E.M., 2000, ApJ, 538, 260–267

Gregersen E.M., Evans N.J., Zhou S.D., Choi M.H., 1997, ApJ, 484, 256–76

Herbst E. & van Dishoeck E. F., 2009, ARA&A, 47, 427

Herbst E., 2008, A&SS, 3.13, 1–3, 129–134

Hogerheijde, M. R., van Dishoeck, E. F., Blake, G. A., & van Langevelde, H. J. 1997, ApJ, 489, 293

Hogerheijde, M. R., van Dishoeck, E. F., Blake, G. A., & van Langevelde, H. J. 1998, ApJ, 502, 315

Kristensen L. E. et al., 2012, A&A, 542, A8

Lada, C. J. 1987, in IAU Symp. 115: Star Forming Regions, ed. M. Peimbert, J. Jugaku, & P. W. J. L. Brand (Reidel, Dordrecht), 1

Mardones, D., Myers, P. C., Tafalla, M., Wilner, D. J., Bachiller, R., & Zhou, S. 1995, ApJ, 442, 685

Myers, P. C., Mardones, D., Tafalla, M., Williams, J. P., & Wilner, D. J. 1996, ApJ, 465, L133

Shu F. H., Adams F. C., Lizano S., 1987, ARA&A, 25, 23

Shu, F. H. 1977, ApJ, 214, 488

Tafalla, M., Mardones, D., Myers, P. C., Caselli, P., Bachiller, R., & Benson, P. J. 1998, ApJ, 504, 900

van Dishoeck E.F., 2009, Astrophysics in the Next Decade, ASS Proceedings, Springer Netherlands, 187

van Dishoeck E. F., 2011, Spring 2011 Lecture Notes, Sterrewacht Leiden

van Dishoeck, E. F. & Blake, G. A. 1998, ARA&A, 36, 317

van Dishoeck, E. F., et al. 1996, A&A, 315, L349

van Dishoeck, E. F. & Hogerheijde, M. R. 1999, The Origins of Stars and Planets, C. J. Lada & N. D. Kylafis, eds., Kluwer Academic Press, Dordrecht (aka Crete II)

van Dishoeck, E. F., Kristensen, L. E., Benz, A. O., et al. 2011, ApJ, 123, 138

van Kempen, T. A., 2008, PhD Thesis, Sterrewacht Leiden

Yıldız, U. A., Kristensen, L. E., van Dishoeck, E. F., et al. 2012, A&A, 521, L40

Appendices